The Astrophysical Journal, 942:111 (18pp), 2023 January 10 https://doi.org/10.3847/1538-4357/aca1c3
© 2023. The Author(s). Published by the American Astronomical Society.
OPEN ACCESS

Pegasus IV: Discovery and Spectroscopic Confirmation of an Ultra-faint Dwarf Galaxy in the Constellation Pegasus

W. Cerny[1,2], J. D. Simon[3], T. S. Li[4], A. Drlica-Wagner[1,2,5], A. B. Pace[6], C. E. Martínez-Vázquez[7,8], A. H. Riley[9,10], B. Mutlu-Pakdil[1,2], S. Mau[11,12], P. S. Ferguson[13], D. Erkal[14], R. R. Munoz[15], C. R. Bom[16], J. L. Carlin[17], D. Carollo[18], Y. Choi[19], A. P. Ji[1,2], V. Manwadkar[2], D. Martínez-Delgado[20], A. E. Miller[21,22], N. E. D. Noël[14], J. D. Sakowska[14], D. J. Sand[23], G. S. Stringfellow[24], E. J. Tollerud[19], A. K. Vivas[8], J. A. Carballo-Bello[25], D. Hernandez-Lang[26], D. J. James[27], D. L. Nidever[28,29], J. L. Nilo Castellon[30,31], K. A. G. Olsen[29], and A. Zenteno[8]
(DELVE Collaboration)
[1] Kavli Institute for Cosmological Physics, University of Chicago, Chicago, IL 60637, USA; williamcerny@uchicago.edu
[2] Department of Astronomy and Astrophysics, University of Chicago, Chicago, IL 60637, USA
[3] Observatories of the Carnegie Institution for Science, 813 Santa Barbara Street, Pasadena, CA 91101, USA
[4] Department of Astronomy and Astrophysics, University of Toronto, 50 St George Street, Toronto ON, M5S 3H4, Canada
[5] Fermi National Accelerator Laboratory, P.O. Box 500, Batavia, IL 60510, USA
[6] McWilliams Center for Cosmology, Carnegie Mellon University, 5000 Forbes Avenue, Pittsburgh, PA 15213, USA
[7] Gemini Observatory, NSF's NOIRLab, 670 North A'ohoku Place, Hilo, HI 96720, USA
[8] Cerro Tololo Inter-American Observatory, NSF's National Optical-Infrared Astronomy Research Laboratory, Casilla 603, La Serena, Chile
[9] George P. and Cynthia Woods Mitchell Institute for Fundamental Physics and Astronomy, Texas A&M University, College Station, TX 77843, USA
[10] Department of Physics and Astronomy, Texas A&M University, College Station, TX 77843, USA
[11] Department of Physics, Stanford University, 382 Via Pueblo Mall, Stanford, CA 94305, USA
[12] Kavli Institute for Particle Astrophysics & Cosmology, P.O. Box 2450, Stanford University, Stanford, CA 94305, USA
[13] Department of Physics, University of Wisconsin-Madison, Madison, WI 53706, USA
[14] Department of Physics, University of Surrey, Guildford GU2 7XH, UK
[15] Departamento de Astronomía, Universidad de Chile, Camino del Observatorio 1515, Las Condes, Santiago, Chile
[16] Centro Brasileiro de Pesquisas Físicas, Rua Doutor Xavier Sigaud 150, 22290-180 Rio de Janeiro, RJ, Brazil
[17] Rubin Observatory/AURA, 950 North Cherry Avenue, Tucson, AZ, 85719, USA
[18] INAF-Osservatorio Astronomico di Trieste, I-34143 Trieste, Italy
[19] Space Telescope Science Institute, 3700 San Martin Drive, Baltimore, MD 21218, USA
[20] Instituto de Astrofísica de Andalucía, CSIC, E-18080 Granada, Spain
[21] Leibniz-Institut für Astrophysik Potsdam (AIP), An der Sternwarte 16, D-14482 Potsdam, Germany
[22] Institut für Physik und Astronomie, Universität Potsdam, Haus 28, Karl-Liebknecht-Straße 24/25, D-14476 Golm (Potsdam), Germany
[23] Department of Astronomy/Steward Observatory, 933 North Cherry Avenue, Room N204, Tucson, AZ 85721-0065, USA
[24] Center for Astrophysics and Space Astronomy, University of Colorado, 389 UCB, Boulder, CO 80309-0389, USA
[25] Instituto de Alta Investigación, Sede Esmeralda, Universidad de Tarapacá, Avenida Luis Emilio Recabarren 2477, Iquique, Chile
[26] Ludwig-Maximilians-Universität München, Scheinerstraße 1, München, Germany
[27] ASTRAVEO, LLC, P.O. Box 1668, Gloucester, MA 01931, USA
[28] Department of Physics, Montana State University, P.O. Box 173840, Bozeman, MT 59717-3840, USA
[29] NSF's National Optical-Infrared Astronomy Research Laboratory, 950 North Cherry Avenue, Tucson, AZ 85719, USA
[30] Departamento de Astronomía, Universidad de La Serena, Avenida Juan Cisternas 1200, La Serena, Chile
[31] Dirección de Investigación y Desarrollo, Universidad de La Serena, Avenida Raúl Bitrán Nachary Nº 1305, La Serena, Chile
Received 2022 March 26; revised 2022 October 23; accepted 2022 November 4; published 2023 January 18

Abstract

We report the discovery of Pegasus IV, an ultra-faint dwarf galaxy found in archival data from the Dark Energy Camera processed by the DECam Local Volume Exploration Survey. Pegasus IV is a compact, ultra-faint stellar system ($r_{1/2} = 41^{+8}_{-6}$ pc; $M_V = -4.25 \pm 0.2$ mag) located at a heliocentric distance of 90^{+4}_{-6} kpc. Based on spectra of seven nonvariable member stars observed with Magellan/IMACS, we confidently resolve Pegasus IV's velocity dispersion, measuring $\sigma_v = 3.3^{+1.7}_{-1.1}$ km s^{-1} (after excluding three velocity outliers); this implies a mass-to-light ratio of $M_{1/2}/L_{V,1/2} = 167^{+224}_{-99} M_\odot/L_\odot$ for the system. From the five stars with the highest signal-to-noise spectra, we also measure a systemic metallicity of $[\mathrm{Fe/H}] = -2.63^{+0.26}_{-0.30}$ dex, making Pegasus IV one of the most metal-poor ultra-faint dwarfs. We tentatively resolve a nonzero metallicity dispersion for the system. These measurements provide strong evidence that Pegasus IV is a dark-matter-dominated dwarf galaxy, rather than a star cluster. We measure Pegasus IV's proper motion using data from Gaia Early Data Release 3, finding $(\mu_{\alpha*}, \mu_\delta) = (0.33 \pm 0.07, -0.21 \pm 0.08)$ mas yr^{-1}. When combined with our measured systemic velocity, this proper motion suggests that Pegasus IV is on an elliptical, retrograde orbit, and is currently near its orbital apocenter. Lastly, we identify three potential RR Lyrae variable stars within Pegasus IV, including one candidate member located more than 10 half-light radii away from the system's centroid. The discovery of yet

Original content from this work may be used under the terms of the Creative Commons Attribution 4.0 licence. Any further distribution of this work must maintain attribution to the author(s) and the title of the work, journal citation and DOI.

another ultra-faint dwarf galaxy strongly suggests that the census of Milky Way satellites is still incomplete, even within 100 kpc.

Unified Astronomy Thesaurus concepts: Galactic archaeology (2178); RR Lyrae variable stars (1410); Dark matter (353); Dwarf galaxies (416); Spectroscopy (1558); Sky surveys (1464)

1. Introduction

Ultra-faint dwarf galaxies represent some of the most extreme galaxies in the known universe: they are the smallest, least luminous, least metal-enriched, and most dark-matter-dominated galaxies yet discovered (e.g., Muñoz et al. 2006; McConnachie 2012; Simon 2019). These systems were formed at high redshift, likely before the epoch of reionization, and thus serve as well-preserved "fossils" that trace the assembly and chemical enrichment histories of their host galaxies (e.g., Bullock & Johnston 2005; Bovill & Ricotti 2009; Frebel 2010; Frebel et al. 2014; Brown et al. 2014). By virtue of their high dark matter content and comparatively minimal baryonic components, these systems are pristine laboratories for studying the nature of dark matter itself. For example, nearby ultra-faint dwarf galaxies are promising sites for the indirect detection of dark matter annihilation or decay through gamma-ray signals (e.g., Ackermann et al. 2014; Albert et al. 2017; Strigari 2018), and the kinematics of stars in these galaxies offer the ability to test the cold dark matter paradigm's prediction for the inner density profile of dark matter halos (e.g., Burkert 1995; Zoutendijk et al. 2021a, 2021b). Additionally, the number and distribution of these systems around the Milky Way can also be leveraged to gain further insight into dark matter microphysics (e.g., Lovell et al. 2012; Bullock & Boylan-Kolchin 2017; Nadler et al. 2021).

The considerable wealth of information about galaxy formation and dark matter encoded in ultra-faint dwarf galaxies has motivated extensive efforts toward their discovery and characterization. Although these galaxies are expected to be the most common class of galaxy by number, their extremely low luminosity has limited their study to the very local universe, where these systems have been discovered exclusively as resolved satellites of the Milky Way, the Magellanic Clouds, and the closest galaxies in the Local Volume (within ∼5 Mpc). Dedicated searches using deep, wide-area photometric catalogs from digital sky surveys have proven to be extremely successful, resulting in the discovery of more than 60 of these systems to date (e.g., Willman et al. 2005; Zucker et al. 2006; Belokurov et al. 2007; Walsh et al. 2007; Belokurov et al. 2014; Kim et al. 2015a; Koposov et al. 2015a; Laevens et al. 2015; Bechtol et al. 2015; Drlica-Wagner et al. 2015; Torrealba et al. 2016; Koposov et al. 2018; Torrealba et al. 2019b). In turn, the characterization of these systems has benefited from follow-up spectroscopy, which can provide robust measurements of the metallicity and mass-to-light ratios of these systems (e.g., Kleyna et al. 2005; Simon & Geha 2007; Kirby et al. 2008; Collins et al. 2013; Simon et al. 2020; Jenkins et al. 2021).

Despite the rapid pace of discoveries in the last two decades, cold dark matter simulations predict that numerous ultra-faint Milky Way satellites remain to be discovered, even in regions of sky covered by previous sky surveys (e.g., Hargis et al. 2014; Newton et al. 2018; Nadler et al. 2020; Manwadkar & Kravtsov 2022). This prediction has recently been affirmed by the discovery of three new Milky Way satellite galaxies by the Hyper Suprime-Cam Subaru Strategic Program (Homma et al. 2016, 2018, 2019) and four additional satellites (including both dwarf galaxy candidates and globular clusters) by the DECam Local Volume Exploration (DELVE; Mau et al. 2020; Cerny et al. 2021a, 2021b; Drlica-Wagner et al. 2021).

In this work, we present the discovery and characterization of yet another ultra-faint Milky Way satellite by DELVE. This new system, Pegasus IV, lies at the very northern edge of sky accessible to the Dark Energy Camera (DECam; Flaugher et al. 2015) in a region previously covered at a shallower depth by the Sloan Digital Sky Survey (SDSS; York et al. 2000 and the Panoramic Survey Telescope and Rapid Response System 1 survey (PS1; Chambers et al. 2016). We use medium-resolution Magellan/Inamori-Magellan Areal Camera and Spectrograph (IMACS) spectroscopy to measure the metallicities and line-of-sight velocities of candidate member stars. We resolve a stellar velocity dispersion and confirm that this system is a dark-matter-dominated ultra-faint dwarf galaxy.

This paper is organized as follows. In Section 2, we describe the DELVE survey, its photometric catalogs, and our ongoing search for undiscovered ultra-faint stellar systems. We also introduce the newly discovered system Pegasus IV. In Section 3, we characterize the morphology and stellar population of Pegasus IV through maximum-likelihood fits to DELVE photometric data. In Section 4, we measure the velocities of stars in the field of Pegasus IV and use the resolved velocity dispersion to infer its mass and dark matter content. We also measure [Fe/H] metallicities and find tentative evidence for a metallicity spread. In Section 5, we discuss the implications of these results for Pegasus IV's classification, leverage Gaia proper motions, and our velocity measurements to constrain its orbit, and highlight the presence of three RR Lyrae (RRL) variable stars. In Section 6, we summarize these results and describe avenues for future study.

2. DELVE Data and Satellite Search

2.1. DELVE Data

The DELVE survey is an ongoing multicomponent observational campaign seeking to achieve deep, contiguous coverage of the high-Galactic-latitude southern sky in the g, r, i, z bands by combining 126 nights of new observations with existing public archival DECam data. DELVE is split into three main survey components dedicated to studying the resolved stellar substructures and satellite populations of the Milky Way (DELVE-WIDE), the Magellanic Clouds (DELVE-MC), and four nearby galaxies with stellar mass similar to the Magellanic Clouds (DELVE-DEEP). To date, DELVE has taken ∼20,000 new exposures toward this goal, and is expected to finish collecting observations in the 2022B semester. A more detailed description of the DELVE science goals, observing strategy, and progress can be found in Drlica-Wagner et al. (2021).

For this work, we used a new internal photometric catalog for DELVE-WIDE covering nearly the entire sky accessible to DECam with $\delta_{J2000} < +30^{\circ}$ and $|b| > 10^{\circ}$, excluding the Dark Energy Survey (DES) footprint. This new catalog will be described in detail in a forthcoming paper (A. Drlica-Wagner et al. 2023, in preparation); we describe the critical components here. We began by selecting all available DELVE and publicly

available exposures with exposure times between 30 and 350 s and effective exposure timescale factors $t_{\rm eff} > 0.3$ (see Neilsen et al. 2015). After this selection, we were left with a total of ∼40,000 exposures, the largest contributors to which were the Dark Energy Camera Legacy Survey (DECaLS; Dey et al. 2019), the DECam eROSITA Survey (DeROSITAS),[32] and DELVE itself. DELVE-WIDE primarily collects g, i band observations, and the r, z data come primarily from the former two survey programs.

We processed all exposures consistently using the DES Data Management Pipeline (DESDM; Morganson et al. 2018), which reduces and detrends DECam images using custom seasonally averaged bias and flat images, and performs background subtraction. Automated source detection and point-spread-function (PSF) photometry was performed on individual reduced CCD images using SourceExtractor (Bertin & Arnouts 1996) and PSFEx (Bertin 2011). Stellar positions were then calibrated against Gaia Data Release 2 (Gaia Collaboration et al. 2018) using `SCAMP` (Bertin 2006), and the photometry was calibrated on a CCD-by-CCD basis using zero-points derived from the ATLAS Refcat2 catalog (Tonry et al. 2018) that were transformed into the DECam photometric system (see Appendix B of Drlica-Wagner et al. 2021). Lastly, the resulting calibrated `SourceExtractor` catalogs for each individual CCD image were merged into a unified multiband object catalog following the procedure introduced in Drlica-Wagner et al. (2015).

Reddening due to interstellar dust was calculated for each object in the resultant catalog from a bilinear interpolation of the maps of Schlegel et al. (1998) with the rescaling from Schlafly & Finkbeiner (2011). Bandpass-specific extinctions were then derived using the coefficients used for DES DR1 (Abbott et al. 2018). Hereafter, we utilize the subscript "0" to denote extinction-corrected magnitudes.

2.2. Satellite Search

We performed a matched-filter search for old, metal-poor stellar systems in the DELVE-WIDE catalog described above using the `simple` algorithm[33] (Bechtol et al. 2015), which has been successfully leveraged to discover more than 20 Milky Way satellites to date. We began by dividing the DELVE-WIDE catalog described in Section 2.1 into HEALPix (Górski et al. 2005) pixels at `NSIDE` = 32 (∼ 3.4 deg^2 pixel^{-1}). For each pixel, we selected stars consistent with an old ($\tau = 12.5$ Gyr), metal-poor ($Z = 0.0001$) PARSEC isochrone (Bressan et al. 2012), which we scanned in distance modulus from 16.0–23.0 mag in intervals of 0.5 mag. Specifically, at each step in the distance modulus grid, we selected all stars with colors consistent with the isochrone locus in color–magnitude space following $\Delta(g-r)_0 < \sqrt{0.1^2 + \sigma_g^2 + \sigma_r^2}$. Stars were defined as sources satisfying the criterion

$$|\texttt{SPREAD\_MODEL\_G}| < 0.003 + \texttt{SPREADERR\_MODEL\_G},$$

where the variable `SPREAD_MODEL` and its associated error, `SPREADERR_MODEL`, are calculated from a likelihood ratio between the best-fitting local PSF model and a more extended model derived from the same PSF model that is additionally convolved with a circular exponential disk model (Desai et al. 2012). After these selections, the resulting filtered stellar density field was smoothed by a 2′ Gaussian kernel, and local density peaks were identified by iteratively raising a density threshold until fewer than 10 distinct peaks remained. Lastly, we computed the Poisson significance of each peak relative to the local background field. Informed by previous searches using `simple`, we inspected diagnostic plots for all candidates above a significance threshold of 5.5σ.

2.3. Discovery of Pegasus IV

During visual inspection of the search results produced by `simple`, we identified a candidate stellar system near ($\alpha_{\rm J2000}$, $\delta_{\rm J2000}$) = (328.°54, 26.°62) at a significance of 6.2σ.[34] Within the candidate pool, this system was exceptional because it appeared to display seven stars at $g_0 \sim 20.5$ spanning a range of photometric color—a feature indicative of a blue horizontal branch (HB). Querying this candidate's centroid in the SIMBAD database (Wenger et al. 2000) revealed the existence of two RRL variable stars within a radius of 2′, both of which were independently identified by the PS1 RRL catalog (Sesar et al. 2017) and the Gaia DR2 variability catalogs (Holl et al. 2018; Clementini et al. 2019).

These identifications strongly merited further investigation of the candidate system. However, the relatively shallow depth of the discovery data was found to be insufficient to draw firm conclusions about the nature and properties of this system. Therefore, we obtained additional g, r, i imaging of the candidate system during regular DELVE observing and in DECam engineering time in 2021 August. These newer observations consisted of 333 s exposures centered on the candidate, improving the depth by ∼0.4 mag in each band compared to the discovery data. These deeper exposures were then incorporated into a newer iteration of the DELVE catalog (prepared identically to the catalog described in Section 2.1), and this newer catalog was used for all analyses and figures in the following sections.

In Figure 1, we present diagnostic plots for the candidate stellar system similar to those generated for each overdensity identified by `simple` . These include the smoothed distribution of isochrone-filtered stars and galaxies (leftmost and center-left panels, respectively), a background-subtracted Hess diagram (center-right panel), and a radial profile for the system (rightmost panel), including the best-fit Plummer (1911) model derived in Section 3.

Our analyses described in the following sections strongly suggest that this system is an ultra-faint dwarf galaxy, rather than a star cluster. Therefore, following the historical naming convention for confirmed dwarf galaxy satellites of the Milky Way, we refer to the system as Pegasus IV throughout this work.

3. Morphological Properties of Pegasus IV

To determine Pegasus IV's morphological properties and the nature of its stellar population, we used the maximum-likelihood approach implemented in the Ultra-faint Galaxy Likelihood toolkit (`ugali`;[35] Bechtol et al. 2015; Drlica-Wagner et al. 2020). Pegasus IV's structure was modeled with a Plummer (1911)

[32] http://astro.userena.cl/derositas/
[33] https://github.com/DarkEnergySurvey/simple
[34] This significance was an underestimate, as a result of a relatively poor initial distance modulus fit from `simple` Our `ugali` likelihood analysis (Section 3) later suggested a test statistic (TS) of TS = 198, corresponding to a Gaussian significance of ∼14.1σ.
[35] https://github.com/DarkEnergySurvey/ugali/

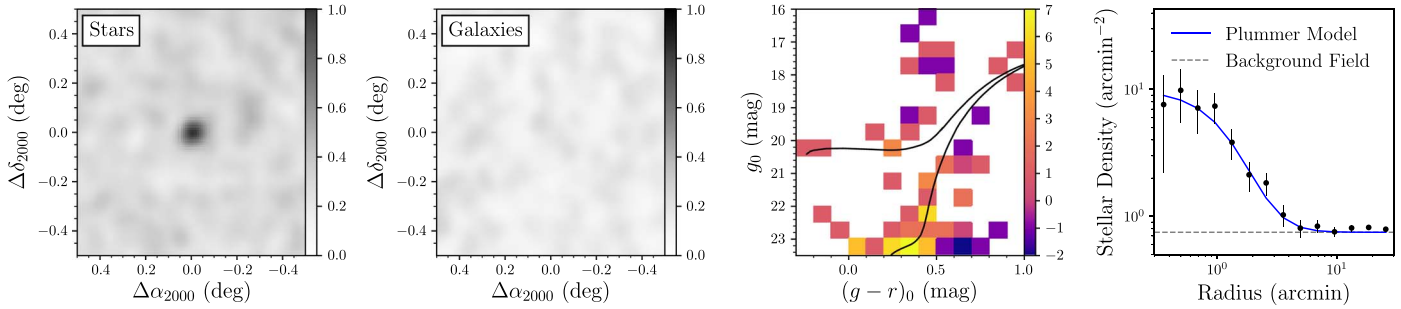

Figure 1. Diagnostic plots for Pegasus IV similar to those visually inspected in the search results from `simple` (except using the DECam follow-up exposures described in Section 2.3). (Left) Smoothed spatial distribution of isochrone-filtered stars within a 0.25 deg^2 region centered on Pegasus IV. (Center left) A similar plot to the leftmost panel, except showing the smoothed spatial distribution of galaxies. (Center right) Hess diagram for a $r_h = 1.6'$ region centered on Pegasus IV after subtracting the background signal from a concentric equal-area annulus at $11r_h$. The best-fit Bressan et al. (2012) isochrone from the `ugali` parameter fit (Section 3) is shown in black. (Right) Radial density profile of stars passing the isochrone filter, assuming spherical symmetry. The errors are derived from the standard deviation of stellar counts in a given annulus divided by the area of that annulus. The best-fit Plummer model (assuming $\epsilon = 0$; see Section 3) is shown in blue. The dashed gray line corresponds to the background field stellar density.

stellar density profile, and a Bressan et al. (2012) isochrone was fit to its observed color–magnitude diagram. We simultaneously constrained the centroid coordinates (α_{2000}, δ_{2000}), angular semimajor axis length (a_h), ellipticity (ϵ), position angle (P.A.) east of north of the Plummer profile and the distance modulus $(m-M)_0$, age (τ), and metallicity (Z) of the isochrone, in addition to the stellar richness (λ), which measures the total number of observable stars in the system. To do so, we explored this multidimensional parameter space using the affine-invariant Markov Chain Monte Carlo (MCMC) sampler `emcee` (Foreman-Mackey et al. 2013), and derived parameter estimates and uncertainties from the median and 16th/84th percentiles of the resulting posterior distributions. Although we later measured a spectroscopic metallicity for the system, we did not fix the metallicity for this parameter fit, both to maintain consistency with the literature and to avoid potential systematic offsets in metallicity between isochrone models and the spectroscopic metallicities.

We report the values associated with each of these parameters, in addition to several properties derived from these results, above the first divider in Table 1. These extra derived properties include the system's azimuthally averaged angular half-light radius (r_h), defined as $r_h = a_h\sqrt{1-\epsilon}$ and the system's absolute magnitude (M_V), integrated stellar luminosity (L_V), and stellar mass (M_*). The absolute V-band magnitude was derived following Martin et al. (2008), and both the stellar mass and stellar luminosity were computed by integrating along the best-fit isochrone assuming a Chabrier (2001) initial mass function.

The results from this parameter fit suggested that Pegasus IV is a relatively small ($r_{1/2} = 41$ pc), round (ellipticity consistent with zero) stellar system at a heliocentric distance of $D_\odot \sim 90$ kpc. In the top left panel of Figure 2, we plot the spatial distribution of stars in a small region centered on Pegasus IV. Stars with `ugali` membership probabilities $p_{\rm ugali} > 5\%$ are colored by their membership probability; stars below this threshold are plotted in gray. Ellipses denoting r_h and $3r_h$ are plotted with a gray dashed line. The bottom left panel displays a color–magnitude diagram covering the same area, with the same color scheme. The best-fit Bressan et al. (2012) isochrone ([Fe/H] $= -1.96$ dex) from the `ugali` fit is shown as a solid black line. While this isochrone is more metal-rich than the spectroscopic metallicity we derive in the following sections, we note that the posterior distribution for the metallicity was bounded below at $Z = 0.0001$ ([Fe/H] $= -2.2$ dex), corresponding to the lowest metallicity in the Bressan et al. (2012) library. The upper limit on Pegasus IV's metallicity from the `ugali` fit was [Fe/H] $= -1.92$ dex (at 95% confidence), and thus our later identification of a lower metallicity for the system is not surprising.

4. Stellar Velocities and Metallicities from Magellan/IMACS Spectroscopy

4.1. Observations and Data Reduction

To confirm that Pegasus IV is a bound stellar system, and to determine its kinematic and dynamical properties, we observed the system with the 6.5 m Magellan-Baade Telescope and IMACS (Dressler et al. 2011) on a two-night observing run spanning 2021 September 12–13. Following previous studies of ultra-faint dwarf galaxies using IMACS, we used the instrument's f/4 camera and the 1200 ℓ mm^{-1} grating blazed at 9000 Å (e.g., Simon et al. 2017). The resulting spectra spanned a wavelength range of ~7500–9000 Å at $R \sim 11{,}000$, sufficient for precise velocity and metallicity measurements from the CaT absorption feature centered at roughly 8500 Å.

We observed a single multislit mask centered on the system, which featured 32 $0\farcs7 \times 5''$ slits. Targets were chosen in the following order. First, we selected red giant branch (RGB) and HB stars consistent with a Dotter (2016) isochrone with age $\tau = 12.5$ Gyr and metallicity [Fe/H] $= -2.3$ in our DECam photometry, informed by past studies of ultra-faint dwarf galaxies. We then added bright stars that we identified as possible members on the basis of a preliminary mixture model analysis of their proper motions in Gaia EDR3 (see Section 4.7). Lastly, to fill remaining available space on the slitmask, we added several stars from Gaia that lacked DECam photometry.

Due to the northern decl. of Pegasus IV ($\delta_{2000} \sim +27°$) and the southern latitude of Las Campanas Observatory, we were only able to observe Pegasus IV at airmass $\lesssim$1.8 with Magellan/IMACS for a little over an hour on each night. On each night, we collected two science exposures ($1800 + 2400$ s), followed by (Kr, Ar, Ne, He) arc lamp calibration frames and flat frames. The typical seeing for these observations was $1\farcs1$ on September 12 and $0\farcs75$ on September 13.

We reduced the IMACS spectroscopic observations following the procedure described by Simon et al. (2017). In brief,

Table 1
Measured and Derived Properties of Pegasus IV

Parameter	Description	Value	Units	Section
α_{2000}	Centroid R.A.	$328.539^{+0.003}_{-0.004}$	deg	3
δ_{2000}	Centroid decl.	$26.620^{+0.003}_{-0.003}$	deg	3
a_h	Angular semimajor axis length	$1.60^{+0.29}_{-0.25}$	arcminutes	3
$a_{1/2}$	Physical semimajor axis length	42^{+8}_{-6}	pc	3
r_h	Azimuthally averaged angular half-light radius	$1.55^{+0.29}_{-0.24}$	arcminutes	3
$r_{1/2}$	Azimuthally averaged physical half-light radius	41^{+8}_{-6}	pc	3
ϵ	Ellipticity	<0.41[a]	...	3
P.A.	Position angle of the major axis (east of north)	115^{+27}_{-41}	deg	3
$(m-M)_0$	Distance modulus	$19.77^{+0.03}_{-0.03} \pm 0.1$[b]	mag	3, 5.5
$D_\odot$	Heliocentric distance	90^{+4}_{-6}	kpc	3
τ	Age	>12.5[c]	Gyr	3
M_V	Absolute (integrated) V-band magnitude	-4.25 ± 0.2[d]	mag	3
L_V	Luminosity	4800^{+800}_{-700}	$L_\odot$	3
M_*	Stellar mass	4400^{+800}_{-600}	$M_\odot$	3
$E(B-V)$	Mean reddening within the half-light radius	0.06	mag	3
$N_{\rm spec}$	Number of spectroscopic members	9	...	4.4
$v_{\rm hel}$	Systemic radial velocity in heliocentric frame	$-273.6^{+1.6}_{-1.5}$	km s^{-1}	4.5
$v_{\rm GSR}$	Systemic radial velocity in the galactic standard of rest	-53.8 ± 1.5	km s^{-1}	4.5
σ_v	Velocity dispersion	$3.3^{+1.7}_{-1.1}$	km s^{-1}	4.5
$M_{1/2}$	Dynamical mass within $r_{1/2}$	$4.0^{+5.1}_{-2.3} \times 10^5$	$M_\odot$	4.5
$M_{1/2}/L_{V,1/2}$	Mass-to-light ratio within $r_{1/2}$	167^{+224}_{-99}	$M_\odot/L_\odot$	4.5
$[{\rm Fe/H}]_{\rm spec}$	Mean spectroscopic metallicity	$-2.67^{+0.25}_{-0.29}$	dex	4.6
$\sigma_{\rm [Fe/H]}$	Metallicity dispersion among spectroscopic members	$0.46^{+0.29}_{-0.17}$	dex	4.6
$\mu_{\alpha*}$	Proper motion in R.A.	0.33 ± 0.07	mas yr^{-1}	4.7
μ_δ	Proper motion in decl.	-0.21 ± 0.08	mas yr^{-1}	4.7
$d_{\rm GC}$	Galactocentric distance	89	kpc	5.2
$r_{\rm apo}$	Orbital apocenter	94^{+8}_{-7}	kpc	5.2
$r_{\rm peri}$	Orbital pericenter	32^{+18}_{-14}	kpc	5.2
e	Orbital eccentricity	$0.49^{+0.17}_{-0.16}$	...	5.2
$\log_{10} J(0.^\circ2)$	Integrated J-factor within a solid angle of $0.^\circ2$	17.8 ± 0.8	GeV^2 cm^{-5}	5.4
$\log_{10} J(0.^\circ5)$	Integrated J-factor within a solid angle of $0.^\circ5$	17.9 ± 0.8	GeV^2 cm^{-5}	5.4

Notes.
[a] The posterior distribution peaked near $\epsilon = 0$. We therefore quote an upper limit at the 95% confidence level.
[b] Following Drlica-Wagner et al. (2015), we assume a systematic uncertainty of ± 0.1 mag on the distance modulus to account for uncertainties in isochrone modeling.
[c] The posterior distribution peaked near $\tau = 13.5$ Gyr, corresponding to the oldest age in our PARSEC isochrone grid. We therefore quote a lower limit at the 95% confidence level.
[d] The uncertainty in the absolute visual magnitude was calculated following Martin et al. (2008) and does not include the uncertainty on the distance.

this process first involved using the Cosmos reduction pipeline (Dressler et al. 2011; Oemler et al. 2017) to map slits on the IMACS detector plane and achieve a preliminary wavelength solution based on the arc lamp data. Then, a modified version of the DEEP2 data reduction pipeline (Cooper et al. 2012; Newman et al. 2013) was used to extract and calibrate the one-dimensional spectrum for each star. We then combined the spectra from the four exposures using inverse-variance weighting.

4.2. Velocity Measurements

We measured stellar radial velocities from the IMACS spectra following the method introduced in Li et al. (2017). This method involves fitting the reduced spectrum of each star with velocity templates by shifting the template through a range of velocities to find the velocity $v_{\rm obs}$ that maximizes the likelihood

$$\mathcal{L} = -\frac{1}{2}\sum_{\lambda=\lambda_1}^{\lambda_2} \frac{\left[f_{\rm spec}(\lambda) - f_{\rm temp}\left(\lambda\left(1+\frac{v_{\rm obs}}{c}\right)\right)\right]^2}{\sigma^2_{\rm spec}}. \quad (1)$$

Here, $f_{\rm spec}(\lambda)$ and $\sigma^2_{\rm spec}(\lambda)$ represent a normalized spectrum and its corresponding variance, and $f_{\rm temp}$ represents a normalized velocity template spectrum. Because we measured velocities specifically from the CaT absorption feature, we set the wavelength bounds of the spectral fit to be $\lambda_1 = 8450$ Å and $\lambda_2 = 8685$ Å. All of our IMACS spectra were fit with three velocity templates: HD122563, a very metal-poor RGB star; HD26297, a more metal-rich RGB star; and HD161817, a blue HB star. We report the velocity measurement from the template that produced the largest likelihood at the best-fit velocity.

For each spectrum-template combination, we ran the MCMC sampler implemented by `emcee` to sample the likelihood

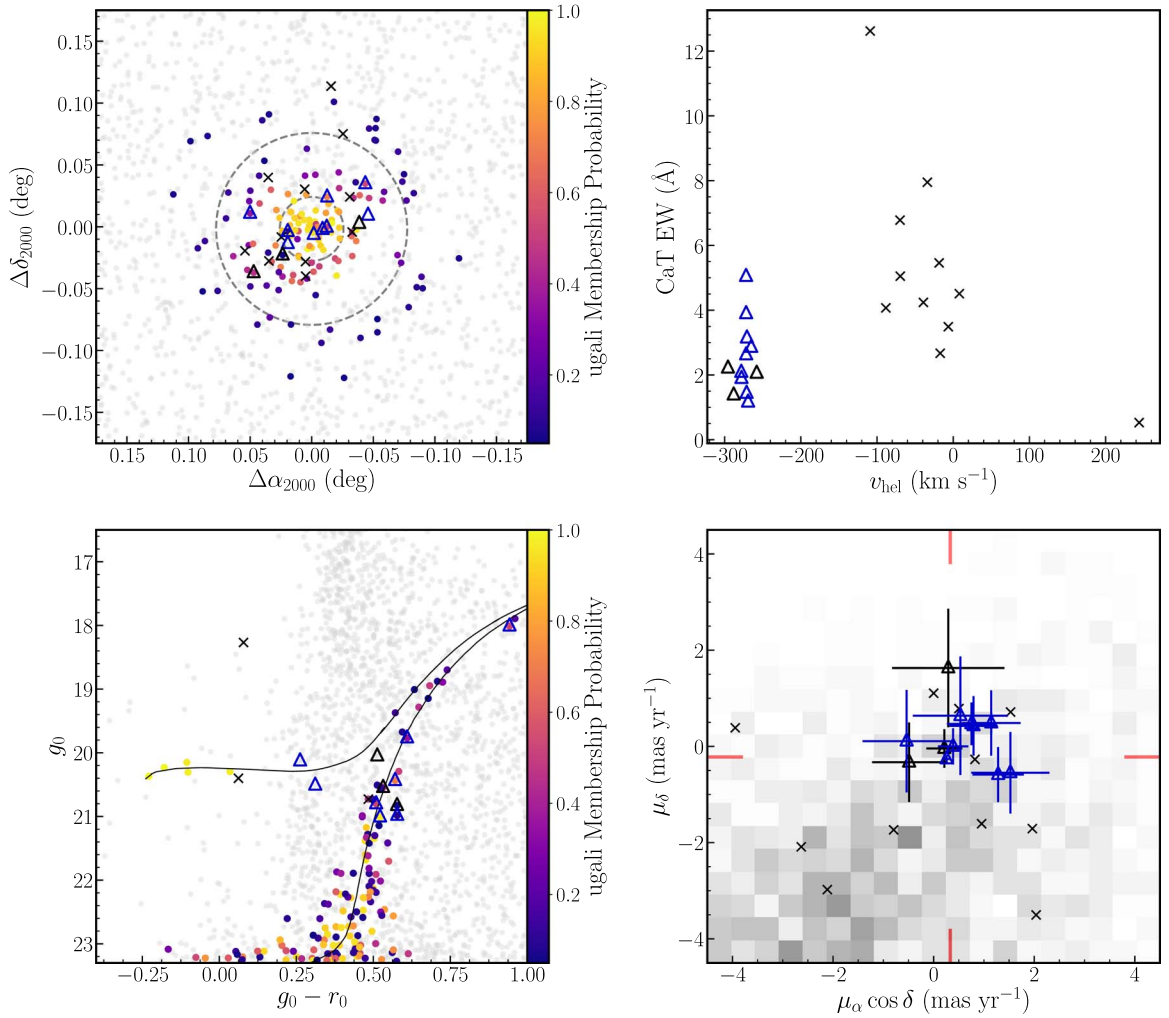

Figure 2. (Top left) Spatial distribution of stars within a small region (radius of ∼0.°25) centered on Pegasus IV. Stars with `ugali` probability $p_{\rm ugali} > 0.05$ are colored by their membership probability, while stars with $p_{\rm ugali} < 0.05$ are colored in gray. Blue triangles denote the nine clear candidate spectroscopic members, while black triangles denote candidate spectroscopic members with uncertain status. Black crosses denote stars observed spectroscopically but deemed nonmembers. Contours representing $1r_{\rm h}$ and $3r_{\rm h}$ are overplotted with a gray dashed line, assuming $\epsilon = 0$ (given the upper limit reported in Table 1). (Top right) calcium triplet equivalent width (CaT EW, in angstroms) vs. heliocentric radial velocity ($v_{\rm hel}$, in kilometers per second) for all 23 stars observed with IMACS at S/N > 3. (Bottom left) Color–magnitude diagram for the same region shown in the top left panel, with the same color/symbol scheme as the preceding panels. The two candidate HB variable stars are seen as blue triangles at g_0–$r_0 \sim 0.25$. One member lacking DECam photometry is excluded here. The majority of nonmembers (especially those selected based on Gaia alone) have redder colors than the axis range shown here. (Bottom right) Gaia proper motions of the stars observed spectroscopically with IMACS, overlaid over a 2D proper motion histogram of all Gaia sources within a radius of ∼0.°25. The candidate spectroscopic members cluster closely near the systemic mean proper motion of $(\mu_{\alpha*}, \mu\delta) = (0.33, -0.22)$ masyr^{-1}, denoted by the red hatches (see Section 4.7).

function above. To ensure robust sampling, we used 25 walkers each taking 2000 steps, with the first 500 steps for each walker discarded as burn-in. Then, for each star, we took the median and the standard deviation (after 5σ clipping) of the velocity posterior distribution for the best-fit template as the measured velocity $v_{\rm obs}$ and velocity error $\sigma_{v_{\rm obs}}$, respectively.

We next applied a telluric correction to this measured velocity $v_{\rm obs}$ to account for the miscentering of stars within slits, which can lead to small (<10 km s^{-1}) offsets in the measured velocities of stars (see e.g., Sohn et al. 2007). To derive the correction for each spectrum, we reran the identical template-fitting MCMC procedure described above except with a telluric template, setting $\lambda_1 = 7550$ Å and $\lambda_2 = 7700$ Å. The median and standard deviation of the resulting posterior distribution then provided the magnitude of the telluric correction $v_{\rm tell}$ and its associated variance $\sigma^2_{v_{\rm tell}}$.

The corrected velocity of each star, v, was calculated as $v = v_{\rm obs} - v_{\rm tell}$ with an associated uncertainty of $\sigma_{v_{\rm stat}} = \sqrt{\sigma^2_{v_{\rm obs}} + \sigma^2_{v_{\rm tell}}}$. The error $\sigma_{v_{\rm stat}}$ is purely statistical in nature, and is directly correlated with the signal-to-noise ratio (S/N) of each individual spectrum. Informed by previous studies that considered the repeatability of IMACS velocities between successive nights (e.g., Simon et al. 2017; Li et al. 2018), we also added a 1.0 km s^{-1} systematic error term in quadrature to each velocity measurement error.

In summary, the above steps resulted in velocities v for each star, each with a single associated uncertainty. These velocities were then transformed into the heliocentric frame. For the rest of this work, we denote the resulting heliocentric velocities as $v_{\rm hel}$. In total, we were able to measure reliable velocities for 23 unique stars at S/N > 3.

4.3. Metallicity Measurements

We measured the metallicity of RGB member stars in Pegasus IV through the equivalent widths (EWs) of the CaT lines. We modeled each of the three CaT lines for each star

Table 2
Properties of Pegasus IV Spectroscopic Member Candidates, Ordered by Decreasing IMACS Spectrum S/N

Gaia EDR3 SourceID	R.A. (deg)	Decl. (deg)	g_0 (mag)	r_0 (mag)	S/N	$v_{\rm hel}$ (km s^{-1})	[Fe/H] (dex)	Comment
1796890071833434112	328.52536	26.62094	18.01	17.07	52.4	-271.9 ± 1.0	$-2.00^{+0.11}_{-0.11}$	RGB
1796887219975171328	328.59498	26.63219	19.77	19.16	10.6	-278.1 ± 1.3	$-2.82^{+0.34}_{-0.41}$	RGB
1796888907896667520	328.48786	26.63070	…[a]	…[a]	7.9	-277.9 ± 1.7	$-2.85^{+0.32}_{-0.40}$	RGB
1796888834882857216	328.49587	26.62398	20.05	19.54	7.8	-257.9 ± 2.0	$-2.77^{+0.31}_{-0.37}$[b]	Binary/nonmember?
1796890381071133568	328.52503	26.64546	20.44	19.87	5.5	-269.2 ± 2.2	$-3.29^{+0.31}_{-0.51}$	RGB
1796890071833414784	328.53716	26.61518	20.13	19.87	4.7	-265.1 ± 1.8	…	HB; variable?
1796886807658193536	328.59171	26.58421	20.54	20.01	4.6	-295.6 ± 2.5	…	Nonmember?
1796887082536156928	328.56077	26.60775	20.51	20.20	3.6	-271.8 ± 3.7	…	HB; RRL
1796891171345139456	328.49033	26.65611	20.80	20.29	3.5	-271.2 ± 4.2	…	RGB
1796887048176397952	328.56543	26.59852	20.83	20.25	3.5	-288.1 ± 2.8	…	Nonmember?
1796887151255658752	328.56076	26.61745	20.98	20.40	3.3	-270.7 ± 3.2	…	RGB
1796890071833423872	328.52913	26.61916	21.00	20.49	3.2	-271.75 ± 3.7	…	RGB

Notes. R.A. and decl. coordinates are taken from Gaia EDR3. The g, r-band photometric measurements are taken from DELVE (with one exception; see below), and correspond to AB magnitudes in the DECam photometric system. The reported S/Ns refer to the IMACS spectroscopic data. The velocity uncertainties reported here include the 1.0 km s^{-1} systematic uncertainty discussed in Section 4.2. We provide a similar table reporting the properties of the spectroscopically observed nonmembers in Appendix B.

[a] This star was not in the DELVE photometric catalog, as it was obscured by a charge-bleed artifact caused by a nearby bright star. For the purpose of deriving this star's [Fe/H] metallicity, we instead calculated a V-band magnitude for this star using the Gaia EDR3 photometry, adopting the transformation relation provided in Table 5.7 of the official Gaia EDR3 documentation; we assumed a conservative error of ±0.1 mag. This magnitude was then used in the Carrera et al. (2013) relation.

[b] This metallicity assumes that the star is a member of Pegasus IV, and therefore that its distance is ∼90 kpc.

with a Gaussian-plus-Lorentzian profile (e.g., Hendricks et al. 2014; Simon et al. 2015), and converted their summed EWs to [Fe/H] metallicities using the calibration relation from Carrera et al. (2013). This relation requires an absolute V-band magnitude for each star, and thus we first converted from the DELVE g, r-band photometry to this system using the relation provided in Bechtol et al. (2015), and then subtracted the distance modulus derived from the `ugali` fit (Section 3). The resulting error on the metallicity for each star was fully propagated from a combination of four sources: (1) uncertainty in the EW measurements, including a 0.2 Å systematic uncertainty floor (Li et al. 2018), (2) uncertainties in the coefficients from the Carrera et al. (2013) relation, (3) uncertainties in the DELVE photometry, and (4) uncertainty associated with the distance modulus from `ugali`. Specifically, we Monte Carlo sampled the posterior distribution associated with each of the above sources of uncertainty, applied the appropriate formulae to calculate [Fe/H] for each set of samples, and then used the median and 16th/84th percentiles of the resultant [Fe/H] samples to define our measurement and 1σ confidence interval for each star. The first of these sources of error is dominant for all but the brightest member star (see Section 4.4).[36]

In general, accurate CaT EW measurements require higher S/N than accurate velocity measurements. Visual inspection of the spectra for stars in our sample revealed that the CaT fits for stars with low S/N were of poor quality, and thus we opted to impose an S/N > 5 cut for metallicity measurements. In total, we measured metallicities for 11 stars above this threshold.

[36] Indeed, switching to the independent CaT EW-[Fe/H] from Starkenburg et al. (2010) produced metallicities consistent within our errors for all member stars with measured metallicities, excluding the brightest one; this star remains consistent at the <2σ level. One member star below the HB was excluded from this comparison, as the Starkenburg et al. (2010) calibration is only defined for stars with $-3 < (V - V_{\rm HB}) < 0$.

4.4. Spectroscopic Membership Determination

From the 23 spectra with S/N > 3 for which we measured velocities, we identified a clear clustering of 12 stars with radial velocities $-300 \lesssim v_{\rm hel} \lesssim -250$ km s^{-1}, including nine within the narrower range of -282 km s$^{-1} \lesssim v_{\rm hel} \lesssim -262$ km s^{-1} (see top right panel of Figure 2). These 12 stars were separated in velocity from all other measured stars with S/N > 3 by a gap of >100 km s^{-1}, and were all located within 4′ (∼2.5r_h) of our derived centroid for Pegasus IV. We summarize the key properties of these 12 stars in Table 2.

To assess which stars among this sample of 12 were plausible Pegasus IV members as opposed to Milky Way contaminants, we subjectively inspected these stars' proper motions from Gaia EDR3, locations in color–magnitude space from the DELVE photometry, and heliocentric velocities and metallicities from the IMACS spectroscopy (where possible). We found that all 12 stars displayed self-consistent proper motions (within 1σ–2σ) and were photometrically consistent with an old, metal-poor isochrone (see bottom panels of Figure 2). Thus, we found no reason to reject any stars as members on the basis of color or proper motion information.

The velocities of these 12 stars appeared to show a considerable spread, ranging from -258 km s$^{-1} \lesssim v_{\rm hel} \lesssim -296$ km s^{-1}. As can be seen in Figure 3, nine of these stars lay within 10 km s^{-1} of the apparent mode near $v_{\rm hel} \sim -272$ km s^{-1}. The remaining three stars fell significantly outside of this range, lying at $v_{\rm hel} \sim [-258, -288, -296]$ km s^{-1}. Even if Pegasus IV truly exhibits a large velocity dispersion, these stars' separation from the peak of the observed velocity distribution suggested that they are either nonmembers or are binary star members of Pegasus IV that were observed at an orbital phase that places them far from their center-of-mass velocity.[37]

The first of the aforementioned velocity outliers (at $v_{\rm hel} \sim -257$ km s^{-1}) was found to have [Fe/H] $= -2.77^{+0.31}_{-0.37}$

[37] No detectable variation in velocity for binary stars is expected in our data between the two successive nights of our observations.

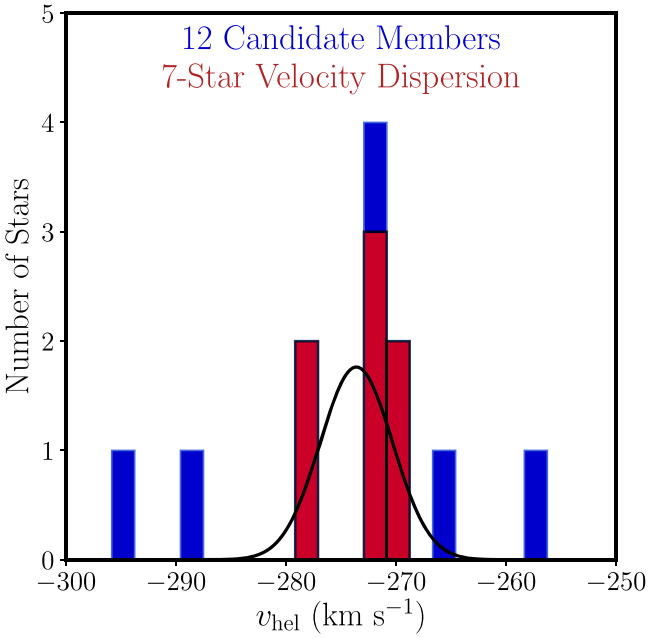

Figure 3. Histogram of radial velocities for the 12 stars identified as candidate members of Pegasus IV (blue), including the seven-star subsample used for our dynamical analysis (red). The best-fit velocity dispersion model, which was derived from those seven stars, is shown as a black Gaussian curve. The two stars that appear consistent with this model, but that are excluded from the red histogram, correspond to the two spectroscopically observed candidate HB variable stars.

dex—consistent with the mean metallicity of this system (see Section 4.6). In general, isolated halo stars at this metallicity are relatively rare (e.g., Schörck et al. 2009; Youakim et al. 2020). Thus, we presume that this star is a candidate binary member star of Pegasus IV, rather than a nonmember, but emphasize that this assumption has a significant impact on the measured velocity dispersion (see Section 4.5). We further caution that the metallicity estimate for this star assumes that the star is located at the distance of Pegasus IV, and will be underestimated should the star prove to be a foreground contaminant. In contrast to the case of the velocity dispersion, however, this star has only a small effect on our estimation of Pegasus IV's metallicity dispersion (see Section 4.6).

For the remaining two velocity outliers, both of which appeared to lie along the RGB of our best-fit isochrone, we were unable to confidently distinguish whether these stars are binary members or foreground nonmembers in the absence of multiepoch velocity measurements. To assess the likelihood that these two stars could be Milky Way foreground contaminants, we ran a simulation using the web interface to the Besançon Galactic model (Robin et al. 2003). We first queried the model to produce a catalog of stellar magnitudes and kinematic measurements for simulated stars within a 1 deg^2 region centered on Pegasus IV. We then transformed the resultant magnitudes from the SDSS photometric system to the DECam photometric system using the equations provided by Drlica-Wagner et al. (2018). Then, we computed the expected surface density of Milky Way stars within a radius of $r < 30'$ that were consistent with the RGB of our target selection isochrone, had heliocentric radial velocities $-300\,{\rm km\,s^{-1}} \leqslant v_{\rm hel} \leqslant -250\,{\rm km\,s^{-1}}$, and had small proper motions ($|\mu| < 4$ mas yr^{-1} in each direction). After multiplying this surface density by the area of the region that the IMACS slitmask covered ($\sim$100 arcmin^2), we found that $\sim$1 foreground star is expected in our spectroscopic sample within this velocity range. Our observation of two stars with outlying radial velocities is slightly inconsistent with this prediction, potentially suggesting that one or both of these stars is a binary member of Pegasus IV. We reiterate that the membership status of these two stars remains highly uncertain.

Lastly, to assess whether the brightest star was indeed a member star despite its relatively high metallicity ([Fe/H] $= -2.00 \pm 0.11$ dex; first row of Table 2), we measured the equivalent width of its Mg I λ8807 Å absorption line. As described by Battaglia & Starkenburg (2012), this line can be used in conjunction with the CaT to discriminate between foreground Milky Way contaminants (primarily main-sequence stars) and dwarf galaxy members (red giants). Fitting the Mg I line with a Gaussian profile, we calculated the equivalent width to be 0.16 ± 0.02 Å (statistical error only). Given the stars CaT equivalent width of $5.1 \pm 0.1 \pm 0.2$ Å , this confidently places the star in the red giant regime defined by Equation (1) of Battaglia & Starkenburg (2012), and thus we concluded that it is very likely that this star is a true RGB member of Pegasus IV.[38]

In summary, we identified nine clear spectroscopic member stars, in addition to one candidate binary member and two potential members with considerably uncertain status. Of the nine clear members, seven are RGB stars, and two appear to lie on the HB. The clear members are shown as blue triangles in Figure 2, while the potential members with uncertain status are shown as black triangles. One of the two spectroscopically observed HB stars is classified as an RRL-type variable in the PS1 and Gaia RRL catalogs (see Section 5.5), and the other appears to show some signs of photometric variability in our data. We include all 12 of these stars in Table 2 as candidate members, but include a comment in the final column to highlight each of the uncertain cases.

4.5. Velocity Dispersion and Mass

To constrain the systemic velocity ($v_{\rm hel}$) and velocity dispersion (σ_v) of Pegasus IV, we sampled the two-parameter Gaussian likelihood function defined by Equation (8) of Walker et al. (2006) using `emcee`. We applied a uniform prior on $v_{\rm hel}$ with a range of [−250, −300] km s^{-1}, and a uniform prior on $\log(\sigma_v)$ with a range of [−2, 2]. For our primary kinematic measurements, we included only the seven clear (nonoutlier) RGB member stars described in Section 4.4. We excluded the two candidate variable stars on the HB from our kinematic sample, since the pulsation of variable stars causes their apparent velocities to vary over time.

Using these seven stars, and applying the priors described above, we measured Pegasus IV's systemic velocity to be $v_{\rm hel} = -273.6^{+1.6}_{-1.5}$ km s^{-1} with a velocity dispersion of $\sigma_v = 3.3^{+1.7}_{-1.1}$ km s^{-1}. The resulting posterior probability distributions from the MCMC sampling are shown in the left panel of Figure 4, and the best-fit model is depicted in black over the velocity histogram in Figure 3. To assess the impact of our prior on this measurement, we also explored adopting a flat

[38] We opted not to conduct a similar analysis on the remaining candidate member stars because of their significantly lower S/N. Furthermore, Battaglia & Starkenburg (2012) suggest that the contaminant/giant populations become less distinguishable in the Mg EW/CaT EW plane for stars with metallicities approaching [Fe/H] $= -3.0$ dex, which would render this approach ineffective for the remaining stars for which we measured S/N > 5 metallicities.

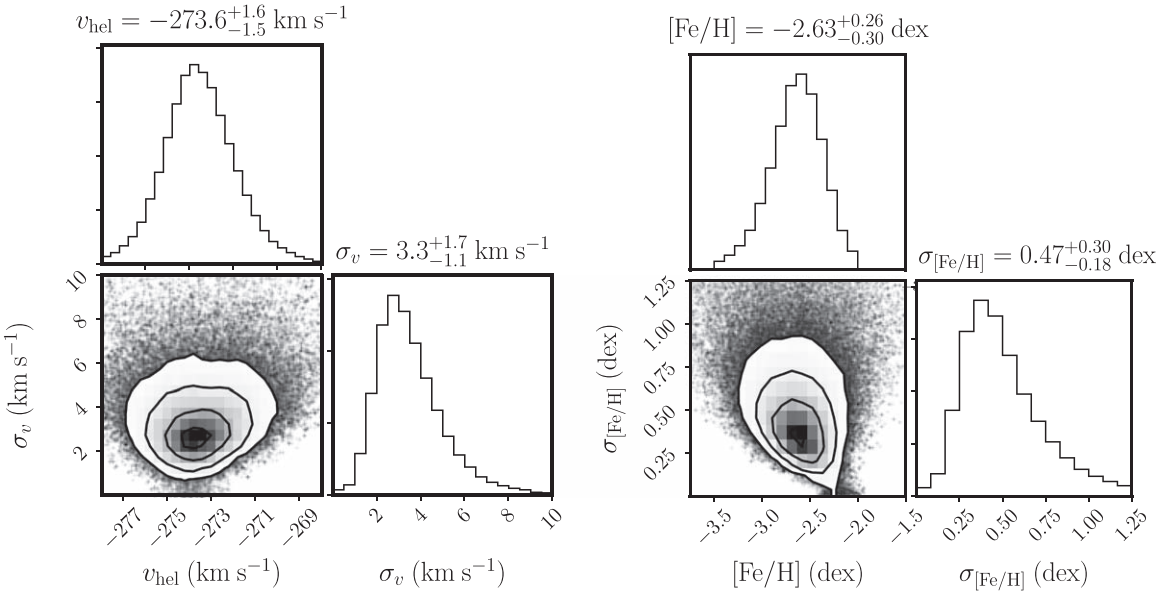

Figure 4. (Left) Two-dimensional posterior probability distributions for the systemic velocity and velocity dispersion, derived through the MCMC sampling procedure described in Section 4.5. (Right) Similar posterior distributions for the metallicity and metallicity dispersion of Pegasus IV (see Section 4.6). The left panel used our nominal sample of seven nonvariable, non-velocity-outlier stars, while the right panel used the five brightest candidate members. Four stars overlap between these samples.

prior on σ_v, rather than $\log(\sigma_v)$. Holding all else constant, this change of prior resulted in changes to the systemic velocity and velocity dispersion that were significantly smaller than the quoted errors of our primary measurements.

Our measured velocity dispersion of $\sigma_v = 3.3^{+1.7}_{-1.1}$ km s^{-1} is clearly nonzero, implying that we confidently resolved the internal dynamics of Pegasus IV. However, the value of this dispersion was found to be sensitive to the exact member used in our velocity dispersion fit. In particular, we observed that including the metal-poor outlier at $v_{\rm hel} \sim -257$ km s^{-1} (while retaining our default priors) raised the velocity dispersion to $\sigma_{v_{\rm hel}} = 6.0^{+2.0}_{-1.3}$ km s^{-1}, consistent within $\lesssim 1.5\sigma$ of the measured dispersion from our nominal seven-star sample. Similarly, including all 12 candidate member stars would raise the velocity dispersion to $\sigma_v = 10.0^{+2.8}_{-1.9}$ km s^{-1} (after relaxing the $\log(\sigma_v)$ prior to $[-3, 3]$). Given that adopting these alternate member samples only increased the resulting velocity dispersion, our primary results derived from the seven-star sample can be considered the most conservative estimate of the dark matter content of Pegasus IV. This ensures that our ultimate conclusion that Pegasus IV is a dark-matter-dominated dwarf galaxy (see Section 5.1) is insensitive to assumptions about the nature of these apparent velocity outliers.

Therefore, under the assumption that Pegasus IV is a dispersion-supported system in dynamical equilibrium, we proceeded to estimate the system's dynamical mass using the mass estimator introduced in Equation (2) of Wolf et al. (2010):

$$M_{1/2} \approx 930 \left(\frac{\sigma_v^2}{\rm km^2\ s^{-2}}\right)\left(\frac{r_{1/2}}{\rm pc}\right) M_\odot. \quad (2)$$

Using our measured dispersion from the nominal seven-star sample and the half-light radius from Section 3, we found Pegasus IV's enclosed mass within $r_{1/2}$ to be $4.0^{+5.1}_{-2.3} \times 10^5 M_\odot$. The mass-to-light ratio within one half-light radius is therefore $M_{1/2}/L_{V,1/2} = 166^{+224}_{-99} M_\odot/L_\odot$.

4.6. Metallicity and Metallicity Spread

To measure Pegasus IV's mean metallicity ($[{\rm Fe/H}]_{\rm spec}$) and metallicity dispersion ($\sigma_{\rm [Fe/H]}$), we applied a simple Gaussian likelihood model that was nearly identical to the model used for the velocity and velocity dispersion. We adopted a uniform prior on $\log(\sigma_{\rm [Fe/H]})$ with a range of $[-2, 2]$, and again performed MCMC sampling using `emcee`. By default, we opted only to use the five stars with S/N > 5 (including the binary candidate at $v_{\rm hel} \sim -257$ km s^{-1}).[39] For these stars, we found $[{\rm Fe/H}]_{\rm spec} = -2.63^{+0.26}_{-0.30}$ dex and metallicity dispersion $\sigma_{\rm [Fe/H]} = 0.47^{+0.30}_{-0.18}$ dex. The resulting posterior probability distributions are shown in the right-hand panel of Figure 4.

Given the small sample of stars with S/N > 5 (five in total), we performed a jackknife test (Efron 1982) to assess the robustness of our measured metallicity and metallicity dispersion. We removed individual stars, one at a time, and reran the MCMC sampling. After doing so, we found that the brightest, most metal-rich star (first row of Table 2) had a particularly strong influence on the metallicity and metallicity dispersion. Removing this star resulted in a more metal-poor systemic mean metallicity of $[{\rm Fe/H}] = -2.91 \pm 0.20$ dex and upper limit on the metallicity dispersion of 0.1 dex (at 84% confidence), in $\sim 2\sigma$ tension with the five-star measurement. By contrast, removing each of the three stars at $[{\rm Fe/H}] \sim -2.82$ dex (second, third, and fourth rows of Table 2) minimally affected the mean metallicity and minorly increased the measured dispersion (at the level of $\sim$0.07 dex, well within the uncertainties on the five-star sample dispersion). Lastly, removing the most metal-poor star (fifth row of Table 2, $[{\rm Fe/H}] \sim -3.3$ dex) increased the mean metallicity to $[{\rm Fe/H}] = -2.45^{+0.21}_{-0.35}$ dex and resulted in a slightly smaller dispersion of $\sigma_{\rm [Fe/H]} = 0.40^{+0.21}_{-0.35}$ dex. Both of these are consistent within 1σ of the five-star result.

These results, in aggregate, suggest that Pegasus IV is a metal-poor stellar system with a tentative detection of a nonzero

[39] The spectra and corresponding CaT fits for each of these stars are shown in Figure 7 in Appendix A.

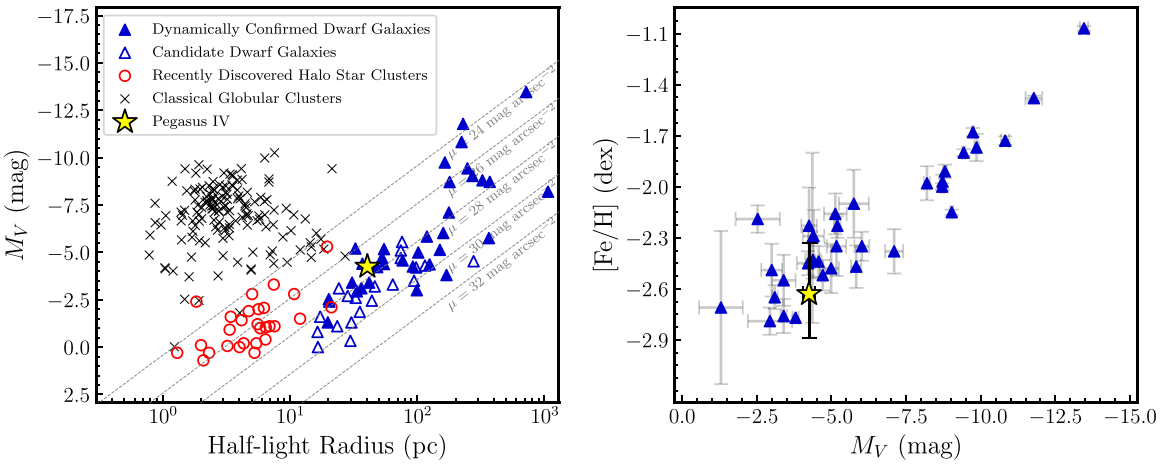

Figure 5. (Left) Absolute V-band magnitude (M_V) vs. azimuthally averaged physical half-light radius ($r_{1/2}$) for the population of known Milky Way globular clusters, faint halo star clusters, and candidate and confirmed dwarf galaxies. Pegasus IV's morphological properties are consistent with the population of candidate and confirmed ultra-faint dwarf galaxies. (Right) Absolute V-band magnitude vs. mean iron abundance ([Fe/H]) for the population of dynamically confirmed ultra-faint dwarf galaxies. Pegasus IV appears to be more metal-poor compared to the population of known dwarfs at the same absolute magnitude, although its mean [Fe/H] metallicity is relatively uncertain. A full reference list for both panels is included in Appendix C.

metallicity dispersion. The magnitude of the dispersion is highly contingent on the membership of the brightest star. Since our measurement of the Mg I λ8807 Å line for this star gives no reason to doubt its membership, we opt to report the metallicity and corresponding dispersion from the five-star sample, namely, $[\mathrm{Fe/H}]_{\mathrm{spec}} = -2.63^{+0.26}_{-0.30}$ dex and $\sigma_{[\mathrm{Fe/H}]} = 0.47^{+0.30}_{-0.18}$ dex, but we emphasize that the value of our measured dispersion is tentative and should be interpreted cautiously due to the small sample size. We also note that this includes the star with a velocity of $v \sim 257$ km s^{-1}, which we assumed to be a true member, but excluded in our kinematic analysis given the likelihood that this star is an unresolved binary.

Regardless of the input stellar sample, the mean metallicity of Pegasus IV places it among the most metal-poor ultra-faint dwarfs known, which include Reticulum III, Bootes II, Tucana II, Horologium I, Draco II, Reticulum II, and Grus I, the metallicities of which range from $-2.81 < [\mathrm{Fe/H}] < -2.62$ dex. Our measurement suggests that Pegasus IV is slightly more metal-poor than other dwarf galaxies of similar absolute magnitude (see the right panel of Figure 5), but this difference does not appear to be statistically significant.

Our measured metallicity dispersion ($\sigma_{[\mathrm{Fe/H}]} = 0.47^{+0.30}_{-0.18}$ dex), while relatively uncertain, is comparable to the dispersions observed in other ultra-faint dwarf galaxies at similar absolute magnitude, i.e., Columba I, Coma Berenices I, Leo V, Pisces II, and Ursa Major II, which have $\sigma_{[\mathrm{Fe/H}]} = 0.71$, 0.43, 0.30, 0.48, and 0.67 dex, respectively (Kirby et al. 2015; Fritz et al. 2019; Simon 2019; Jenkins et al. 2021). Pegasus IV's metallicity dispersion can also be compared to the intrinsic iron abundance spreads observed in the Milky Way's (bright) globular cluster population, which Bailin (2019) found to have a median metallicity dispersion of $\sigma_{[\mathrm{Fe/H}]}$=0.045 dex across a sample of 55 clusters with high-resolution spectra.

4.7. Proper Motion

We computed the systemic proper motion of Pegasus IV using the precise astrometry provided by Gaia EDR3 (Gaia Collaboration et al. 2021). We analyzed three different proper motion models to measure the systemic proper motion. The first was a mixture model composed of dwarf and Milky Way components and utilizes spatial position and proper motion (Pace & Li 2019; Pace et al. 2022). This model was run prior to the acquisition of both deeper photometry and spectroscopy, and its results informed our spectroscopic target selection. It was run with preliminary spatial parameters and only used stars with DECam photometry. With this model, we found $\mu_{\alpha*} = 0.39 \pm 0.17$ mas yr^{-1} and $\mu_\delta = 0.01 \pm 0.18$ mas yr^{-1}. The model also reports the number of probable members with proper motion measurements, which was found to be $N = 12.3 \pm 1.4$ stars. Due to the color–magnitude selection window, this model missed the brightest member, which explains the worse precision compared to the following models.

The second proper motion model was similar to the first, but used only a fixed sample of spectroscopic members as input. We used a multivariate Gaussian distribution to model the dwarf, and we sampled the posterior probability using `emcee`. With this model, we found $\mu_{\alpha*} = 0.33 \pm 0.07$ mas yr^{-1}, $\mu_\delta = -0.21 \pm 0.08$ mas yr^{-1}, assuming a fixed sample of $N = 9$ stars (consisting of the seven stars used for the dynamical analysis, in addition to the two spectroscopically observed variable star candidates).

The third model used a similar mixture model, but built on those of Pace & Li (2019) and Pace et al. (2022) by incorporating spectroscopic information. We preassigned the membership of stars with spectroscopy, which assists in determining both the dwarf and Milky Way proper motion distributions. We did not exclude stars missing DECam photometry and instead applied a loose Gaia color–magnitude selection for these stars. With this model, we found $\mu_{\alpha*} = 0.33 \pm 0.07$ mas yr^{-1} and $\mu_\delta = -0.22 \pm 0.08$ mas yr^{-1}, and $N = 13.1 \pm 0.6$. The proper motion from this model is almost identical to the spectroscopic member-only results from the second model, likely because the additional members are generally faint (mostly HB stars) and do not significantly influence the measurement. We note that the majority of the systemic proper motion precision comes from the brightest member. The proper motion error of this star is $\sigma_{\mu_{\alpha*}} = 0.08$ mas yr^{-1} (similar to the systemic proper motion error) and its inclusion decreases the systemic proper motion error by ~40%. We opted to use the systemic proper motion derived from the spectroscopic members as our preferred measurement

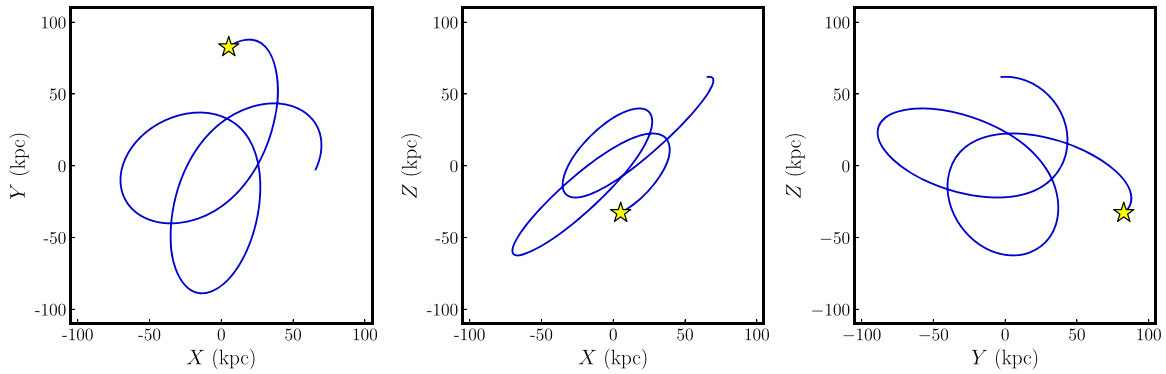

Figure 6. Projections of Pegasus IV's fiducial orbit for the last 5 Gyr in the Galactocentric *X-Y*, *X-Z*, and *Y-Z* planes (left, center, and right panels, respectively). Pegasus IV's current position is depicted as a gold star.

for further analysis of Pegasus IV's kinematics, since this measurement is least likely to be biased by contaminant stars. We do note, however, that differences have been observed between dwarf galaxy proper motions derived from spectroscopic samples and those derived without (e.g., Massari & Helmi 2018).

5. Discussion

5.1. Classification of Pegasus IV

Recent discoveries of ultra-faint Milky Way satellites have broadly consisted of two classes of objects: dark-matter-dominated dwarf galaxies and likely baryon-dominated halo star clusters. We find that Pegasus IV is significantly more consistent with the former class of objects on the basis of its size, mass-to-light ratio, and metallicity dispersion. Specifically, Pegasus IV's half-light radius is larger than the population of known globular clusters (see the left panel of Figure 5). More conclusively, Pegasus IV's large mass-to-light ratio ($M_{1/2}/L_{V,1/2} = 167^{+224}_{-99}\,M_\odot/L_\odot$) is inconsistent with the known population of halo star clusters, which typically exhibit mass-to-light ratios of $\sim$1–3 $M_\odot/L_\odot$ (e.g., Dalgleish et al. 2020). Lastly, the system's tentatively resolved metallicity dispersion suggests that it has undergone multiple generations of star formation and/or that its gravitational potential well is deep enough to have retained supernova ejecta, both of which are indicative of a dark-matter-dominated dwarf galaxy (e.g., Willman & Strader 2012).

We note that the conclusion that Pegasus IV is an ultra-faint dwarf galaxy could be further tested in the future through higher-resolution spectroscopic observations of its bright member stars. Such spectra would allow for measurements of the galaxy's α-element and neutron-capture element abundances, both of which can independently offer further insight into the classification of this system (e.g., Ji et al. 2019). Alternately, deeper medium-resolution spectra could provide iron abundances for a large sample of stars, allowing for a more robust measurement of the system's metallicity dispersion.

5.2. Orbit

To determine Pegasus IV's orbital properties, we integrated 500 realizations of its orbit using the `gala` Python package (Price-Whelan 2017). For each realization, we determined Pegasus IV's initial conditions $\{\alpha_{J2000}, \delta_{J2000}, D_\odot, \mu_{\alpha*}, \mu_\delta, v_\odot\}$ by sampling from the error distributions of its observed position and kinematics (Table 1), which we approximated as Gaussian for all parameters. We then rewound Pegasus IV's orbit back in time for 5 Gyr in the presence of `gala`'s default Milky Way model, which includes a spherical nucleus and bulge, a Miyamoto–Nagai disk (Miyamoto & Nagai 1975), and a spherical Navarro–Frenk–White (NFW) dark matter halo (Navarro et al. 1996).

At the conclusion of each integration, we recorded `gala`'s estimate for Pegasus IV's apocenter (r_{apo}), pericenter (r_{peri}), eccentricity (e), orbital angular momentum perpendicular to the Galactic disk (L_z), and total energy (E). From the median and 16th/84th percentiles of the distributions for these quantities across the 500 realizations, we find

1. $r_{apo} = 94^{+8}_{-7}$ kpc $\quad r_{peri} = 32^{+18}_{-14}$ kpc
2. $e = 0.49^{+0.17}_{-0.16}$
3. $L_z = 6.3^{+2.9}_{-2.6}$ kpc^2 Myr^{-1}
4. $E = -0.049^{+0.005}_{-0.004}$ kpc^2 Myr^{-2}.

In Figure 6, we depict the last 5 Gyr of Pegasus IV's orbit (in various projections) assuming the velocity, distance, and proper motions reported in Table 1 as initial conditions. Notably, the model predicted that Pegasus IV passed its apocenter within the last $\sim$200 Myr and experienced its last pericentric passage $\sim$1 Gyr ago.

To contextualize Pegasus IV's proximity to its orbital apocenter, we computed the ratio: $f = (d_{GC} - r_{peri})/(r_{apo} - r_{peri})$ following Fritz et al. (2018). This ratio quantifies a satellite's proximity to its pericenter ($f = 0$) or apocenter ($f = 1$). Assuming Pegasus IV's distance to the Galactic center is $d_{GC} = 89$ kpc and adopting the apocenter/pericenter distances given above, we found $f = 0.92$. This value for the ratio f places Pegasus IV in a regime that is underpopulated compared to the predictions from simple orbital dynamics (e.g., see Figure 5 of Li et al. 2022). Our discovery of Pegasus IV in a previously surveyed region of the sky may support the hypothesis that the dearth of known Milky Way satellite galaxies observed near their apocenters ($f \sim 1$) is an observational selection effect (e.g., Fritz et al. 2018; Simon 2018; Li et al. 2022, although see Pace et al. 2022 for a more detailed discussion of this hypothesis).

5.3. Association with Local Group Structures

A number of recently discovered ultra-faint dwarf galaxies have been proposed to be associated with the Large Magellanic Cloud (LMC; e.g., Koposov et al. 2015a; Drlica-Wagner et al. 2015; Erkal & Belokurov 2020; Patel et al. 2020; Correa Magnus & Vasiliev 2022). To assess whether Pegasus IV is a

satellite of the LMC, we rewound the system in the combined presence of the LMC and Milky Way potential using the technique described in Erkal & Belokurov (2020). For the Milky Way potential, we used the potential fits of McMillan (2017). We note that we did not select the highest likelihood potential but instead sampled the Milky Way from the posterior chains of McMillan (2017) to account for uncertainties in the potential. We modeled the LMC as a Hernquist profile (Hernquist 1990) with a mass of $1.38 \times 10^{11} M_{\odot}$ and a scale radius of 16.08 kpc, motivated by the results of Erkal et al. (2019). In these simulations, we treated the LMC and Milky Way as particles sourcing their respective potentials and thus account for the reflex motion of the Milky Way in response to the LMC (e.g., Gómez et al. 2015). We modeled the dynamical friction of the Milky Way on the LMC using the approximations in Jethwa et al. 2016. For the LMC's present-day proper motions, distance, and radial velocity we used values provided by Kallivayalil et al. (2013), Pietrzyński et al. 2019, and van der Marel et al. (2002), respectively.

In order to account for uncertainties, we Monte Carlo sampled the present-day observables of Pegasus IV, the Milky Way potential, and the LMC's present-day observables 10,000 times and rewound the satellite for 5 Gyr.[40] We computed the energy of Pegasus IV relative to the LMC 5 Gyr ago (as in Erkal & Belokurov 2020), and found that Pegasus IV has a 0.07% chance of having originally been energetically bound to the LMC, suggesting that it is not an LMC satellite. We also considered the approach of Patel et al. (2020) and determined the closest passage of Pegasus IV to the LMC and compared their relative speed to the escape speed of the LMC. With this approach, we found that Pegasus IV passes the LMC at 61 ± 12 kpc, with a relative speed of 363 ± 19 km s^{-1}. This is $\sim$3 times the escape speed of the LMC, which also suggests that Pegasus IV is not an LMC satellite.

A substantial fraction of the known Milky Way satellite galaxies lies on a thin, corotating plane nearly perpendicular to the Milky Way's stellar disk dubbed the Vast Polar Structure (VPOS; Pawlowski et al. 2012, 2015; Fritz et al. 2018; Li et al. 2021). Adopting the same VPOS parameters as Li et al. (2021), namely, the assumed normal $(l_{\rm MW}, b_{\rm MW}) = (169.^{\circ}3, -2.^{\circ}8)$ and angular tolerance $\theta_{\rm inVPOS} = 36.^{\circ}87$, we found it unlikely that Pegasus IV is a VPOS member. The observed angle between the VPOS and the satellite's orbital pole is $\theta_{\rm VPOS} = 52.3^{+19.8}_{-19.5}$ and the probability that the orbital pole lies within $\theta_{\rm inVPOS}$ of the VPOS normal is $\sim$20%. While this does not rule out the possibility that Pegasus IV is a VPOS member, the currently available phase space measurements do not favor this scenario.

Lastly, we considered whether Pegasus IV might be associated with debris from the Sagittarius dwarf spheroidal galaxy (Sgr dSph) and its extended stellar stream. Considering the Sgr dSph model and associated coordinate system from Law & Majewski (2010), we found that Pegasus IV is located at an angle of $\beta = -52.^{\circ}9$ from the Sgr dSph debris plane. We found a comparably large separation when considering the newer Sgr dSph model from Vasiliev et al. (2021), who additionally incorporated the impact of the LMC when modeling the Sgr dSph's debris stream. We therefore conclude that Pegasus IV is unlikely to be associated with the Sgr dSph.

[40] This model produced estimates for Pegasus IV's apocenter and pericenter that agreed with the results from the Milky Way potential-only integration (Section 5.2) to well within the quoted uncertainties reported in Table 1.

5.4. Astrophysical J-factor/D-factor

The Milky Way dwarf spheroidal satellite galaxies are excellent targets for searches for dark matter annihilation or decay products due to their close proximity, astrophysical backgrounds, and large mass-to-light ratios (e.g., Ackermann et al. 2015). The astrophysical component of the dark matter flux from annihilation (decay) is known as the J-factor (D-factor) and depends on the squared (linear) dark matter density along the line of sight. Our framework to calculate J-factors and D-factors follows Pace & Strigari (2019) and is similar to other previous analyses of dSph galaxies (e.g., Bonnivard et al. 2015; Geringer-Sameth et al. 2015). Briefly, we solved for the velocity dispersion in the spherical Jeans equations and compared it to the velocity dispersion from the spectroscopic members to determine the dark matter density profile. We assumed the dark-matter-dominated mass follows an NFW profile, while the stellar distribution follows a Plummer profile. We assumed that stellar anisotropy is constant with radius. We used the results derived in Section 3 for the distance, structural parameters (a_h, ϵ), and associated uncertainties, which were transformed into Gaussian priors. For more details, see Pace & Strigari (2019).

We applied this methodology to the same seven-star (nonvariable) member sample used for our dynamical analysis in Section 4.5. We calculated integrated J-factors of $\log_{10} J = 17.7 \pm 0.8$, 17.8 ± 0.8, 17.9 ± 0.8 for solid angles of $\theta = 0.^{\circ}1$, $0.^{\circ}2$, $0.^{\circ}5$ in logarithmic units of GeV^2 cm^{-5}. The integrated D-factors are $\log_{10} D = 16.9 \pm 0.4$, 17.3 ± 0.5, 17.8 ± 0.6 for solid angles of $\theta = 0.^{\circ}1$, $0.^{\circ}2$, and $0.^{\circ}5$ in logarithmic units of GeV cm^{-2}. The predicted J-factor is $\log_{10} J(0.^{\circ}5s) \sim 17.6$ based on velocity dispersion, heliocentric distance, and half-light radius scaling relations and agrees with the full dynamical analysis (Pace & Strigari 2019). This J-factor is not large compared to other ultra-faint dwarfs due primarily to the relatively large distance of Pegasus IV. We note that if Pegasus IV were located at its pericenter ($d = 32$ kpc), its J-factor would be comparable to the largest J-factors measured for other dwarf galaxies: $\log_{10} J(0.^{\circ}5) \sim 18.8$.

5.5. Distance from Two RR Lyrae Variable Stars

RRL-type variable stars are excellent tracers of old, metal-poor stellar populations in the Milky Way halo, and have been identified in nearly every ultra-faint dwarf galaxy (e.g., Greco et al. 2008; Boettcher et al. 2013; Medina et al. 2017; Joo et al. 2018, 2019; Martínez-Vázquez et al. 2019; Vivas et al. 2020; Martínez-Vázquez et al. 2021). According to the empirical relation derived by Martínez-Vázquez et al. (2019), ultra-faint dwarf galaxies with the same absolute magnitude as Pegasus IV ($M_V = -4.25$) are expected to have between two and four RRLs.

As introduced in Section 2.3, we identified two RRLs in the Gaia and PS1 RRL catalogs within a $2'$ radius of Pegasus IV's centroid at the time of discovery. The first of these stars (Gaia DR2/EDR3 `SOURCE_ID`: 1796887082536156928; Gaia $G = 20.08$ mag) was labeled as an RRab star in both catalogs with a period of 0.7088 days (averaging between the individual catalogs, which agreed at the level of 0.0001 days). This star was identified as a spectroscopic member in Section 4.4 on the basis of its radial velocity. The second of these stars (Gaia DR2/EDR3 `SOURCE_ID`: 1796890209272433792; $G = 20.24$ mag) was labeled as an RRc-type variable with a period of

0.31373 days (again averaging between Gaia and PS1, which agreed within 0.00001 days for this star); we do not have a spectrum for this star.

Under the assumption that these stars were bona fide RRL member stars of Pegasus IV, we estimated their absolute magnitudes using the empirical calibration given in Muraveva et al. (2018):

$$M_G = (0.32 \pm 0.04)[\mathrm{Fe/H}] + (1.11 \pm 0.06). \quad (3)$$

Assuming that the (unknown) RRL metallicities are sampled from the Pegasus IV metallicity distribution function, which we approximate as a Gaussian centered on $[\mathrm{Fe/H}] = -2.63$ dex with variance $\sigma = 0.47$ dex, we found that the expected absolute magnitude of the two stars is $M_G = 0.26^{+0.18}_{-0.20}$ mag, where the uncertainties include contributions from both the sampled RRL metallicity and the errors associated with the coefficients in the Muraveva et al. (2018) relation. From this absolute magnitude, the resulting distance modulus for each of the RRLs was then derived from

$$(m - M)_0 = G - (R_G \times (E(B - V)) - M_G, \quad (4)$$

where R_G is the ratio of total-to-selective absorption for the Gaia G filter, which we assumed to be $R_G = 2.45$ (Wang & Chen 2019). Taking $E(B-V) = 0.06$ mag for both stars (Table 1), we found $(m - M)_0 = 19.66^{+0.20}_{-0.18}$ from the first RRL and for the second, neglecting the errors on G and $E(B-V)$ as they were subdominant to the error on M_G. The average of these distance moduli is $(m-M)_0 = 19.74 \pm 0.13$, in excellent agreement with the distance modulus derived from isochrone fitting, $(m-M)_0 = 19.77 \pm 0.03$ (stat) ± 0.1 (sys) (Section 3).

5.6. A Distant RRL Member?

The Gaia and PS1 RRL catalogs include an additional RRL located at $(\alpha_{J2000}, \delta_{J2000}) = (328.^{\circ}834, 26.^{\circ}602)$, corresponding to a 15.8′ separation from Pegasus IV's centroid, or roughly 10 half-light radii (∼0.42 kpc). This star (Gaia DR2/EDR3 SOURCE_ID: 1796879729552126080; Gaia $G = 20.12$ mag) was flagged in the PS1 catalog as an RRc with a period $P = 0.400555$ days. Its Gaia EDR3 proper motion $(\mu_{\alpha}{}^{*}, \mu_{\delta}) = (+0.114 \pm 0.460, -0.328 \pm 0.541)$ mas yr^{-1} is consistent with the systemic mean proper motion derived in Section 4.7: $(+0.33 \pm 0.07, -0.21 \pm 0.08)$ mas yr^{-1}. The distance modulus of this star according to the Muraveva et al. (2018) relation is $(m - M)_0 = 19.70^{+0.20}_{-0.18}$, lying between the distance moduli derived for the other two RRLs discussed in the previous section, and in equally good agreement with the distance modulus derived through isochrone fitting.

These properties suggest that this RRL may be related to Pegasus IV, despite its extreme angular separation. To quantify the possibility that this star is a field RRL, as opposed to a true Pegasus IV member, we integrated the RRL number density radial profile given in Medina et al. (2018) between Galactocentric distances of 80 and 100 kpc. We found that only 0.0075 RRL stars are expected in a 0.25 deg^2 region around Pegasus IV. Thus, it is very unlikely that this star is a field star, as opposed to a true Pegasus IV member.

RRLs with large angular separations have been observed in the vicinity of several ultra-faint dwarf galaxies (e.g., Vivas et al. 2020; Stringer et al. 2021), and have been proposed to be tidally stripped members of these galaxies.[41] To assess whether tidal stripping is needed to explain the position of this RRL relative to Pegasus IV, we calculated the system's Jacobi radius following Equation (8.91) of Binney & Tremaine (2008). As explained by Binney & Tremaine (2008), the Jacobi radius approximately corresponds to the expected maximum observed extent of a satellite system in a circular orbit. Adopting the dynamical and structural properties from Table 1, and assuming the simple power-law Milky Way potential from Eadie & Harris (2016), we found that the Jacobi radius for Pegasus IV is ∼0.6 kpc—larger than the projected separation of this RRL from the main body of Pegasus IV (∼0.42 kpc). However, if we instead perform this calculation assuming that Pegasus IV is at its pericenter distance ($r_{\mathrm{peri}} = 32$ kpc), the Jacobi radius is found to be ∼0.26 kpc, smaller than the observed projected separation. We note, though, that these Jacobi radii are significant underestimates, as they are calculated using the dynamical mass within $r_{1/2}$ in absence of a total mass estimate for Pegasus IV.

This latter Jacobi radius estimate admits the possibility that the distant RRL was tidally stripped from the main body of Pegasus IV at a previous pericentric passage, although the close clustering of the confirmed spectroscopic members somewhat disfavors this interpretation. Ultimately, it is difficult to confirm or dispute this star's connection to Pegasus IV without a radial velocity measurement. Wider-area spectroscopic member samples may allow for searches for features suggestive of tidal disruption (e.g., velocity gradients), which would add credence to the tidal origin of this distant star if present. Improved distance estimation for each of the RRLs may also offer further insight into the consistency of this star with the majority of Pegasus IV's members.

Lastly, we note also that there may be yet more RRL members of Pegasus IV, as the Gaia and PS1 RRL catalogs are incomplete at faint magnitudes (e.g., Mateu et al. 2020). Our team has recently obtained deeper Gemini North/GMOS imaging of Pegasus IV (GN-2021B-FT-111; PI: C. Martinez-Vazquez). We therefore defer a more extensive search for RRLs in the central region of Pegasus IV to a future study leveraging these data. These new data will also help disambiguate the nature of the second spectroscopically observed HB star, which appeared to show some signs of variability in the sparsely sampled DELVE data.

6. Summary

We have presented the discovery of Pegasus IV, an ultra-faint dwarf galaxy found in a wide-area search of DELVE data. Through a maximum-likelihood fit to the system's morphology and observed color–magnitude diagram, we found that Pegasus IV is an old, metal-poor stellar system with a half-light radius of $r_{1/2} = 41$ pc and an absolute magnitude of $M_V = -4.25$. With Magellan/IMACS medium-resolution spectra for a small sample of member stars, we resolved the internal kinematics of the system, finding a velocity dispersion of $\sigma_v = 3.3^{+1.7}_{-1.1}$ km s^{-1}, implying a mass-to-light ratio for the system of $M_{1/2}/L_{V,1/2} = 167^{+224}_{-99} M_{\odot}/L_{\odot}$. We used the CaT absorption lines in the same spectra to derive iron abundances for five stars, which suggested that Pegasus IV is very

[41] We also note that Chiti et al. (2021) discovered and confirmed multiple member stars at extremely large separations from the Tucana II dwarf galaxy, highlighting that yet more member stars may be discoverable in the outskirts of Pegasus IV.

metal-poor ([Fe/H] = −2.63) and exhibits a metallicity spread that further suggests its nature as a dwarf galaxy. We also measured Pegasus IV's proper motion using data from Gaia EDR3, which, in conjunction with the system's measured velocity of $v_{\rm hel} = -273.6\,{\rm km\,s^{-1}}$, suggested that Pegasus IV is on a retrograde orbit, and just passed its orbital apocenter. Lastly, we constrained the distance to Pegasus IV using a metallicity–absolute magnitude relation for two RR Lyrae stars found in the system, confirming that the system is located at a heliocentric distance of ∼90 kpc as determined through isochrone fitting.

Our discovery of Pegasus IV in data from DECam is consistent with the prediction that many ultra-faint Milky Way satellites remain to be discovered, not only in previously unsearched regions, but also in regions of sky previously covered by current-generation surveys. Survey efforts including DELVE-WIDE will likely continue to play an important role in this ongoing satellite census. Illustratively, Manwadkar & Kravtsov (2022) recently forecasted that DELVE-WIDE may discover 34^{+17}_{-13} ultra-faint dwarf galaxies with $M_V < 0$ and $r_{1/2} > 10\,{\rm pc}$ across its nominal footprint ($\delta_{2000} < 0°$; $|b| > 10°$), assuming that DELVE will achieve comparable sensitivity to searches over third-year DES data (Drlica-Wagner et al. 2020). Furthermore, the upcoming Vera C. Rubin Observatory Legacy Survey of Space and Time (Ivezić et al. 2019) is expected to discover hundreds of ultra-faint dwarf galaxies both around the Milky Way and beyond (e.g., Hargis et al. 2014; Trujillo et al. 2021; Mutlu-Pakdil et al. 2021; Manwadkar & Kravtsov 2022). This growing sample of ultra-faint dwarf galaxies will undoubtedly provide new constraints on the properties of dark matter and will offer key insight into the process of galaxy formation on the smallest scales.

The DELVE project is partially supported by Fermilab LDRD project L2019-011 and the NASA Fermi Guest Investigator Program Cycle 9 No. 91201. W.C. gratefully acknowledges support from the University of Chicago Quad Undergraduate Research Scholars program and from the Carnegie Astrophysics Summer Student Internship (CASSI) program, during which training in spectroscopic data analysis was acquired. A.B.P. acknowledges support from NSF grant AST-1813881. C.E.M.-V. is supported by the international Gemini Observatory, a program of NSF's NOIRLab, which is managed by the Association of Universities for Research in Astronomy (AURA) under a cooperative agreement with the National Science Foundation, on behalf of the Gemini partnership of Argentina, Brazil, Canada, Chile, the Republic of Korea, and the United States of America. B.M.P. is supported by an NSF Astronomy and Astrophysics Postdoctoral Fellowship under award AST-2001663. This research received support from the National Science Foundation (NSF) under grant no. NSF DGE-1656518 through the NSF Graduate Research Fellowship received by S.M. R.R.M. gratefully acknowledges support by the ANID BASAL project FB210003. J.A.C.-B. acknowledges support from ANID FONDECYT Regular 1220083.

This project used data obtained with the Dark Energy Camera (DECam), which was constructed by the Dark Energy Survey (DES) Collaboration. Funding for the DES Projects has been provided by the DOE and NSF (USA), MISE (Spain), STFC (UK), HEFCE (UK), NCSA (UIUC), KICP (U. Chicago), CCAPP (Ohio State), MIFPA (Texas A&M University), CNPQ, FAPERJ, FINEP (Brazil), MINECO (Spain), DFG (Germany), and the collaborating institutions in the Dark Energy Survey, which are Argonne Lab, UC Santa Cruz, University of Cambridge, CIEMAT-Madrid, University of Chicago, University College London, DES-Brazil Consortium, University of Edinburgh, ETH Zürich, Fermilab, University of Illinois, ICE (IEEC-CSIC), IFAE Barcelona, Lawrence Berkeley Lab, LMU München, and the associated Excellence Cluster Universe, University of Michigan, NSF's National Optical-Infrared Astronomy Research Laboratory, University of Nottingham, Ohio State University, OzDES Membership Consortium University of Pennsylvania, University of Portsmouth, SLAC National Lab, Stanford University, University of Sussex, and Texas A&M University.

This work has made use of data from the European Space Agency (ESA) mission Gaia (https://www.cosmos.esa.int/gaia), processed by the Gaia Data Processing and Analysis Consortium (DPAC; https://www.cosmos.esa.int/web/gaia/dpac/consortium). Funding for the DPAC has been provided by national institutions, in particular the institutions participating in the Gaia Multilateral Agreement.

Based on observations at Cerro Tololo Inter-American Observatory, NSF's National Optical-Infrared Astronomy Research Laboratory (2019A-0305; PI: Drlica-Wagner), which is operated by the Association of Universities for Research in Astronomy (AURA) under a cooperative agreement with the National Science Foundation.

This research has made use of NASA's Astrophysics Data System Bibliographic Services.

This manuscript has been authored by Fermi Research Alliance, LLC, under contract No. DE-AC02-07CH11359 with the US Department of Energy, Office of Science, Office of High Energy Physics. The United States Government retains and the publisher, by accepting the article for publication, acknowledges that the United States Government retains a nonexclusive, paid-up, irrevocable, worldwide license to publish or reproduce the published form of this manuscript, or allow others to do so, for United States Government purposes.

Supported by the international Gemini Observatory, a program of NSF's NOIRLab, which is managed by the Association of Universities for Research in Astronomy (AURA) under a cooperative agreement with the National Science Foundation, on behalf of the Gemini partnership of Argentina, Brazil, Canada, Chile, the Republic of Korea, and the United States of America.

Facilities: Blanco, Gaia, Magellan-IMACS.

Software: `SourceExtractor` (Bertin & Arnouts 1996) `PSFEx` (Bertin 2011), `emcee` (Foreman-Mackey et al. 2013), `gala` (Price-Whelan 2017), `HEALPix` (Górski et al. 2005),[42] `healpy`,[43] `ugali` (Bechtol et al. 2015),[44] `simple` (Bechtol et al. 2015).[45]

Appendix A
CaT Fits for Member Stars with Measured Metallicities

In Figure 7, we show our fits to the calcium triplet lines of the five stars for which we reported metallicities (top five rows of Table 2). In each panel, we specifically plot the normalized

[42] http://healpix.sourceforge.net
[43] https://github.com/healpy/healpy
[44] https://github.com/DarkEnergySurvey/ugali
[45] https://github.com/DarkEnergySurvey/simple

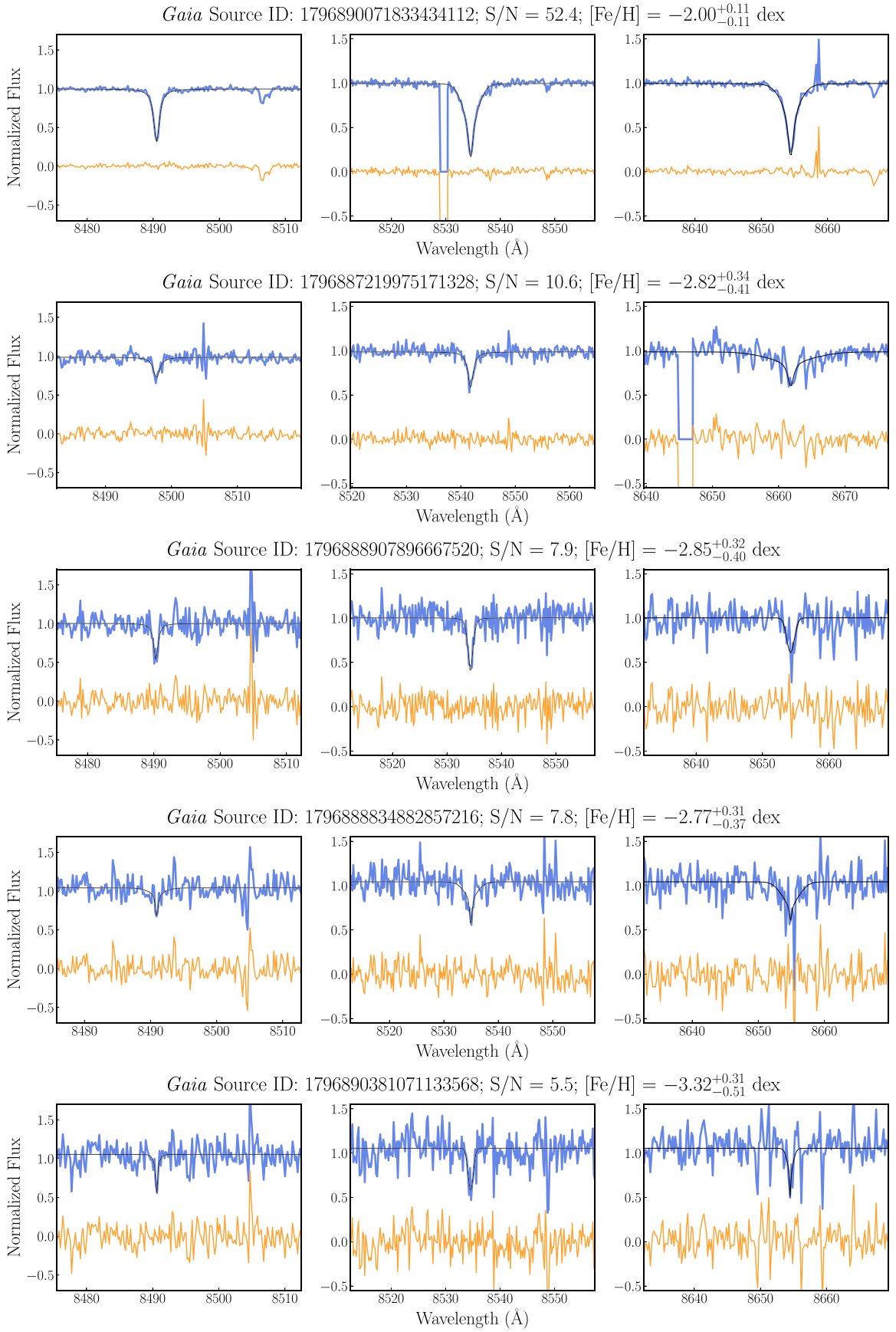

Figure 7. Spectra for the five stars with S/N > 5 for which we measured metallicities.

spectrum of each star in blue, the best-fit model in black, and include the residuals for these fits in orange. For some stars, rectangular features in the spectra (associated with chip gaps) and/or residual emission-like or absorption-like features (associated with imperfect sky line subtraction) are visible. We note that wavelength ranges with chip gaps were masked during the fitting process, and therefore had no influence on the resulting fits.

Appendix B
Properties of Spectroscopically Observed Nonmembers in the Field of Pegasus IV

In Table 3, we report the properties of 11 nonmember stars in the field of Pegasus IV for which we obtained an IMACS spectrum at $S/N > 3$. All 11 stars are clearly excluded from membership in Pegasus IV on the basis of their radial velocities.

Appendix C
References for the Literature Data Presented in Figure 5

The left panel of Figure 5 shows the populations of "classical" Milky Way globular clusters, recently discovered halo star clusters, and dwarf galaxies in the M_V–$r_{1/2}$ plane. The globular cluster measurements are taken from Harris (1996). The faint star cluster measurements are taken from Fadely et al. (2011), Balbinot et al. (2013), Kim et al. (2015b), Kim et al. (2016a), Weisz et al. (2016), Martin et al. (2016), Luque et al. (2017), Muñoz et al. (2018), Luque et al. (2018), Conn et al. (2018), Longeard et al. (2019), Torrealba et al. (2019a), Mau et al. (2019), Homma et al. (2019), Mau et al. (2020), and Gatto et al. (2021). We also include the DELVE 2 stellar system (Cerny et al. 2021a) in this category, although this system's true classification remains unknown.

The dwarf galaxy measurements for the same panel are taken from McConnachie (2012), Koposov et al. (2015a), Martin et al. (2015), Kim & Jerjen (2015), Kim et al. (2016b),

Table 3
Properties of 11 Nonmember Stars in the Field of Pegasus IV, Ordered by Decreasing IMACS Spectrum S/N

Gaia EDR3 SourceID	R.A. (deg)	Decl. (deg)	g_0 (mag)	r_0 (mag)	S/N	v_{hel} (km s^{-1})	Σ EW (Å)
1796890277991932672	328.54542	26.65170	18.27	18.19	18.0	-17.1 ± 1.6	2.7 ± 0.3
1796886876377693184	328.57785	26.59370	21.56	20.16	9.4	-18.5 ± 1.9	5.5 ± 0.6
1796885570707607552	328.54452	26.58141	21.95	20.57	7.3	8.0 ± 2.2	4.5 ± 1.2
1796885570708834816	328.54467	26.59317	22.53	21.12	6.3	-6.5 ± 2.4	3.5 ± 0.7
1796887082537343488	328.56656	26.61302	21.80	20.48	6.3	-88.4 ± 2.5	4.1 ± 0.8
1796890419725155840	328.50446	26.64552	21.82	20.54	5.4	-69.8 ± 2.7	6.8 ± 1.6
1796891411863389696	328.51056	26.69646	22.14	20.83	4.6	-39.2 ± 2.8	⋯
1796888628724409344	328.50228	26.61709	20.73	20.24	4.0	-108.9 ± 2.3	⋯
1796890625885606400	328.57853	26.66116	21.45	20.43	3.8	-69.5 ± 4.0	⋯
1796886910737451520	328.59964	26.60191	21.76	20.60	3.6	-34.0 ± 4.2	⋯
1796892034634891264	328.52139	26.73499	20.40	20.34	3.0	244.0 ± 6.3	⋯

Note. Refer to Table 2 for the details of each column. We report the summed EW of the three CaT lines (Σ EW) for each star with $S/N > 5$; we could not derive [Fe/H] metallicities for these stars because their distances are unknown. The corresponding uncertainties reported for Σ EW include the 0.2 Å systematic uncertainty discussed in Section 4.3.

Crnojević et al. (2016), Torrealba et al. (2016), Carlin et al. (2017), Muñoz et al. (2018), Torrealba et al. (2018), Homma et al. (2018), Mutlu-Pakdil et al. (2018), Longeard et al. (2018), Torrealba et al. (2019b), Homma et al. (2019), Wang et al. (2019), Simon et al. (2020), Moskowitz & Walker (2020), Mau et al. (2020), Cantu et al. (2021), and Cerny et al. (2021b).

The right panel of the same figure shows the [Fe/H]$-r_{1/2}$ plane, including only dynamically confirmed Milky Way dwarf galaxies (solid blue triangles in the left panel). The metallicity measurements for these systems are taken from Carlin et al. (2009), Simon et al. (2015), Willman et al. (2011), Koposov et al. (2015b), Kirby et al. (2015), Torrealba et al. (2016), Kim et al. (2016b), Li et al. (2017), Caldwell et al. (2017), Li et al. (2018), Koposov et al. (2018), Torrealba et al. (2019b), Simon (2019), Simon et al. (2020), Pace et al. (2020), Chiti et al. (2021), Jenkins et al. (2021), and Longeard et al. (2022).

ORCID iDs

W. Cerny https://orcid.org/0000-0003-1697-7062
J. D. Simon https://orcid.org/0000-0002-4733-4994
T. S. Li https://orcid.org/0000-0002-9110-6163
A. Drlica-Wagner https://orcid.org/0000-0001-8251-933X
A. B. Pace https://orcid.org/0000-0002-6021-8760
C. E. Martínez-Vázquez https://orcid.org/0000-0002-9144-7726
A. H. Riley https://orcid.org/0000-0001-5805-5766
B. Mutlu-Pakdil https://orcid.org/0000-0001-9649-4815
S. Mau https://orcid.org/0000-0003-3519-4004
P. S. Ferguson https://orcid.org/0000-0001-6957-1627
D. Erkal https://orcid.org/0000-0002-8448-5505
R. R. Munoz https://orcid.org/0000-0002-0810-5558
C. R. Bom https://orcid.org/0000-0003-4383-2969
J. L. Carlin https://orcid.org/0000-0002-3936-9628
D. Carollo https://orcid.org/0000-0003-4710-132X
Y. Choi https://orcid.org/0000-0003-1680-1884
A. P. Ji https://orcid.org/0000-0002-4863-8842
D. Martínez-Delgado https://orcid.org/0000-0003-3835-2231
A. E. Miller https://orcid.org/0000-0002-7483-7327
N. E. D. Noël https://orcid.org/0000-0002-8282-469X
J. D. Sakowska https://orcid.org/0000-0002-1594-1466
D. J. Sand https://orcid.org/0000-0003-4102-380X
G. S. Stringfellow https://orcid.org/0000-0003-1479-3059
E. J. Tollerud https://orcid.org/0000-0002-9599-310X
A. K. Vivas https://orcid.org/0000-0003-4341-6172
J. A. Carballo-Bello https://orcid.org/0000-0002-3690-105X
D. J. James https://orcid.org/0000-0001-5160-4486
D. L. Nidever https://orcid.org/0000-0002-1793-3689
K. A. G. Olsen https://orcid.org/0000-0002-7134-8296
A. Zenteno https://orcid.org/0000-0001-6455-9135

References

Abbott, T. M. C., Abdalla, F. B., Allam, S., et al. 2018, ApJS, 239, 18
Ackermann, M., Albert, A., Anderson, B., et al. 2014, PhRvD, 89, 042001
Ackermann, M., Albert, A., Anderson, B., et al. 2015, PhRvL, 115, 231301
Albert, A., Anderson, B., Bechtol, K., et al. 2017, ApJ, 834, 110
Bailin, J. 2019, ApJS, 245, 5
Balbinot, E., Santiago, B. X., da Costa, L., et al. 2013, ApJ, 767, 101
Battaglia, G., & Starkenburg, E. 2012, A&A, 539, A123
Bechtol, K., Drlica-Wagner, A., Balbinot, E., et al. 2015, ApJ, 807, 50
Belokurov, V., Irwin, M. J., Koposov, S. E., et al. 2014, MNRAS, 441, 2124
Belokurov, V., Zucker, D. B., Evans, N. W., et al. 2007, ApJ, 654, 897
Bertin, E. 2006, in ASP Conf. Ser. 351, Astronomical Data Analysis Software and Systems XV, ed. C. Gabriel et al. (San Francisco, CA: ASP), 112
Bertin, E. 2011, in ASP Conf. Ser. 442, Astronomical Data Analysis Software and Systems XX, ed. I. N. Evans et al. (San Francisco, CA: ASP), 435
Bertin, E., & Arnouts, S. 1996, A&AS, 117, 393
Binney, J., & Tremaine, S. 2008, Galactic Dynamics (2nd ed.; Princeton, NJ: Princeton Univ. Press)
Boettcher, E., Willman, B., Fadely, R., et al. 2013, AJ, 146, 94
Bonnivard, V., Combet, C., Maurin, D., & Walker, M. G. 2015, MNRAS, 446, 3002
Bovill, M. S., & Ricotti, M. 2009, ApJ, 693, 1859
Bressan, A., Marigo, P., Girardi, L., et al. 2012, MNRAS, 427, 127
Brown, T. M., Tumlinson, J., Geha, M., et al. 2014, ApJ, 796, 91
Bullock, J. S., & Boylan-Kolchin, M. 2017, ARA&A, 55, 343
Bullock, J. S., & Johnston, K. V. 2005, ApJ, 635, 931
Burkert, A. 1995, ApJL, 447, L25
Caldwell, N., Walker, M. G., Mateo, M., et al. 2017, ApJ, 839, 20
Cantu, S. A., Pace, A. B., Marshall, J., et al. 2021, ApJ, 916, 81
Carlin, J. L., Grillmair, C. J., Muñoz, R. R., Nidever, D. L., & Majewski, S. R. 2009, ApJL, 702, L9
Carlin, J. L., Sand, D. J., Muñoz, R. R., et al. 2017, AJ, 154, 267
Carrera, R., Pancino, E., Gallart, C., & del Pino, A. 2013, MNRAS, 434, 1681
Cerny, W., Pace, A. B., Drlica-Wagner, A., et al. 2021a, ApJ, 910, 18
Cerny, W., Pace, A. B., Drlica-Wagner, A., et al. 2021b, ApJL, 920, L44
Chabrier, G. 2001, ApJ, 554, 1274
Chambers, K. C., Magnier, E. A., Metcalfe, N., et al. 2016, arXiv:1612.05560
Chiti, A., Frebel, A., Simon, J. D., et al. 2021, NatAs, 5, 392
Clementini, G., Ripepi, V., Molinaro, R., et al. 2019, A&A, 622, A60
Collins, M. L. M., Chapman, S. C., Rich, R. M., et al. 2013, ApJ, 768, 172
Conn, B. C., Jerjen, H., Kim, D., & Schirmer, M. 2018, ApJ, 852, 68
Cooper, M. C., Newman, J. A., Davis, M., Finkbeiner, D. P., & Gerke, B. F. 2012, spec2d: DEEP2 DEIMOS Spectral Pipeline, Astrophysics Source Code Library, ascl:1203.003
Correa Magnus, L., & Vasiliev, E. 2022, MNRAS, 511, 2610
Crnojević, D., Sand, D. J., Zaritsky, D., et al. 2016, ApJL, 824, L14
Dalgleish, H., Kamann, S., Usher, C., et al. 2020, MNRAS, 492, 3859
Desai, S., Armstrong, R., Mohr, J. J., et al. 2012, ApJ, 757, 83
Dey, A., Schlegel, D. J., Lang, D., et al. 2019, AJ, 157, 168
Dotter, A. 2016, ApJS, 222, 8
Dressler, A., Bigelow, B., Hare, T., et al. 2011, PASP, 123, 288
Drlica-Wagner, A., Bechtol, K., Mau, S., et al. 2020, ApJ, 893, 47
Drlica-Wagner, A., Bechtol, K., Rykoff, E. S., et al. 2015, ApJ, 813, 109
Drlica-Wagner, A., Carlin, J. L., Nidever, D. L., et al. 2021, ApJS, 256, 2
Drlica-Wagner, A., Sevilla-Noarbe, I., Rykoff, E. S., et al. 2018, ApJS, 235, 33
Eadie, G. M., & Harris, W. E. 2016, ApJ, 829, 108
Efron, B. 1982, The Jackknife, the Bootstrap and Other Resampling Plans (Philadelphia, PA: Society for Industrial and Applied Mathematics)
Erkal, D., & Belokurov, V. A. 2020, MNRAS, 495, 2554
Erkal, D., Belokurov, V., Laporte, C. F. P., et al. 2019, MNRAS, 487, 2685
Fadely, R., Willman, B., Geha, M., et al. 2011, AJ, 142, 88
Flaugher, B., Diehl, H. T., Honscheid, K., et al. 2015, AJ, 150, 150
Foreman-Mackey, D., Hogg, D. W., Lang, D., & Goodman, J. 2013, PASP, 125, 306
Frebel, A. 2010, AN, 331, 474
Frebel, A., Simon, J. D., & Kirby, E. N. 2014, ApJ, 786, 74
Fritz, T. K., Battaglia, G., Pawlowski, M. S., et al. 2018, A&A, 619, A103
Fritz, T. K., Carrera, R., Battaglia, G., & Taibi, S. 2019, A&A, 623, A129
Gaia Collaboration, Brown, A. G. A., Vallenari, A., et al. 2018, A&A, 616, A1
Gaia Collaboration, Brown, A. G. A., Vallenari, A., et al. 2021, A&A, 649, A1
Gatto, M., Ripepi, V., Bellazzini, M., et al. 2021, RNAAS, 5, 159
Geringer-Sameth, A., Koushiappas, S. M., & Walker, M. 2015, ApJ, 801, 74
Gómez, F. A., Besla, G., Carpintero, D. D., et al. 2015, ApJ, 802, 128
Górski, K. M., Hivon, E., Banday, A. J., et al. 2005, ApJ, 622, 759
Greco, C., Dall'Ora, M., Clementini, G., et al. 2008, ApJL, 675, L73
Hargis, J. R., Willman, B., & Peter, A. H. G. 2014, ApJL, 795, L13
Harris, W. E. 1996, AJ, 112, 1487
Hendricks, B., Koch, A., Walker, M., et al. 2014, A&A, 572, A82
Hernquist, L. 1990, ApJ, 356, 359
Holl, B., Audard, M., Nienartowicz, K., et al. 2018, A&A, 618, A30
Homma, D., Chiba, M., Komiyama, Y., et al. 2019, PASJ, 71, 94
Homma, D., Chiba, M., Okamoto, S., et al. 2016, ApJ, 832, 21
Homma, D., Chiba, M., Okamoto, S., et al. 2018, PASJ, 70, S18
Ivezić, Ž., Kahn, S. M., Tyson, J. A., et al. 2019, ApJ, 873, 111
Jenkins, S. A., Li, T. S., Pace, A. B., et al. 2021, ApJ, 920, 92
Jethwa, P., Erkal, D., & Belokurov, V. 2016, MNRAS, 461, 2212

Ji, A. P., Simon, J. D., Frebel, A., Venn, K. A., & Hansen, T. T. 2019, ApJ, 870, 83
Joo, S.-J., Kyeong, J., Yang, S.-C., et al. 2018, ApJ, 861, 23
Joo, S.-J., Kyeong, J., Yang, S.-C., et al. 2019, ApJ, 875, 120
Kallivayalil, N., van der Marel, R. P., Besla, G., Anderson, J., & Alcock, C. 2013, ApJ, 764, 161
Kim, D., & Jerjen, H. 2015, ApJL, 808, L39
Kim, D., Jerjen, H., Mackey, D., Da Costa, G. S., & Milone, A. P. 2015a, ApJL, 804, L44
Kim, D., Jerjen, H., Milone, A. P., Mackey, D., & Da Costa, G. S. 2015b, ApJ, 803, 63
Kim, D., Jerjen, H., Mackey, D., Da Costa, G. S., & Milone, A. P. 2016a, ApJ, 820, 119
Kim, D., Jerjen, H., Geha, M., et al. 2016b, ApJ, 833, 16
Kirby, E. N., Simon, J. D., & Cohen, J. G. 2015, ApJ, 810, 56
Kirby, E. N., Simon, J. D., Geha, M., Guhathakurta, P., & Frebel, A. 2008, ApJL, 685, L43
Kleyna, J. T., Wilkinson, M. I., Evans, N. W., & Gilmore, G. 2005, ApJL, 630, L141
Koposov, S. E., Belokurov, V., Torrealba, G., & Evans, N. W. 2015a, ApJ, 805, 130
Koposov, S. E., Casey, A. R., Belokurov, V., et al. 2015b, ApJ, 811, 62
Koposov, S. E., Walker, M. G., Belokurov, V., et al. 2018, MNRAS, 479, 5343
Laevens, B. P. M., Martin, N. F., Ibata, R. A., et al. 2015, ApJL, 802, L18
Law, D. R., & Majewski, S. R. 2010, ApJ, 714, 229
Li, H., Hammer, F., Babusiaux, C., et al. 2021, ApJ, 916, 8
Li, T. S., Ji, A. P., Pace, A. B., et al. 2022, ApJ, 928, 30
Li, T. S., Simon, J. D., Drlica-Wagner, A., et al. 2017, ApJ, 838, 8
Li, T. S., Simon, J. D., Pace, A. B., et al. 2018, ApJ, 857, 145
Longeard, N., Martin, N., Ibata, R. A., et al. 2019, MNRAS, 490, 1498
Longeard, N., Martin, N., Starkenburg, E., et al. 2018, MNRAS, 480, 2609
Longeard, N., Jablonka, P., Arentsen, A., et al. 2022, MNRAS, 516, 2348
Lovell, M. R., Eke, V., Frenk, C. S., et al. 2012, MNRAS, 420, 2318
Luque, E., Pieres, A., Santiago, B., et al. 2017, MNRAS, 468, 97
Luque, E., Santiago, B., Pieres, A., et al. 2018, MNRAS, 478, 2006
Manwadkar, V., & Kravtsov, A. 2022, MNRAS, 516, 3944
Martin, N. F., de Jong, J. T. A., & Rix, H.-W. 2008, ApJ, 684, 1075
Martin, N. F., Nidever, D. L., Besla, G., et al. 2015, ApJL, 804, L5
Martin, N. F., Jungbluth, V., Nidever, D. L., et al. 2016, ApJL, 830, L10
Martínez-Vázquez, C. E., Vivas, A. K., Gurevich, M., et al. 2019, MNRAS, 490, 2183
Martínez-Vázquez, C. E., Cerny, W., Vivas, A. K., et al. 2021, AJ, 162, 253
Massari, D., & Helmi, A. 2018, A&A, 620, A155
Mateu, C., Holl, B., De Ridder, J., & Rimoldini, L. 2020, MNRAS, 496, 3291
Mau, S., Drlica-Wagner, A., Bechtol, K., et al. 2019, ApJ, 875, 154
Mau, S., Cerny, W., Pace, A. B., et al. 2020, ApJ, 890, 136
McConnachie, A. W. 2012, AJ, 144, 4
McMillan, P. J. 2017, MNRAS, 465, 76
Medina, G. E., Muñoz, R. R., Vivas, A. K., et al. 2017, ApJL, 845, L10
Medina, G. E., Muñoz, R. R., Vivas, A. K., et al. 2018, ApJ, 855, 43
Miyamoto, M., & Nagai, R. 1975, PASJ, 27, 533
Morganson, E., Gruendl, R. A., Menanteau, F., et al. 2018, PASP, 130, 074501
Moskowitz, A. G., & Walker, M. G. 2020, ApJ, 892, 27
Muñoz, R. R., Carlin, J. L., Frinchaboy, P. M., et al. 2006, ApJL, 650, L51
Muñoz, R. R., Côté, P., Santana, F. A., et al. 2018, ApJ, 860, 66
Muraveva, T., Delgado, H. E., Clementini, G., Sarro, L. M., & Garofalo, A. 2018, MNRAS, 481, 1195
Mutlu-Pakdil, B., Sand, D. J., Carlin, J. L., et al. 2018, ApJ, 863, 25
Mutlu-Pakdil, B., Sand, D. J., Crnojević, D., et al. 2021, ApJ, 918, 88
Nadler, E. O., Wechsler, R. H., Bechtol, K., et al. 2020, ApJ, 893, 48
Nadler, E. O., Drlica-Wagner, A., Bechtol, K., et al. 2021, PhRvL, 126, 091101
Navarro, J. F., Frenk, C. S., & White, S. D. M. 1996, ApJ, 462, 563
Neilsen, E., Bernstein, G., Gruendl, R., & Kent, S. 2015, Limiting Magnitude, τ, $T_{\rm eff}$, and image quality in DES Year 1, Tech. Rep., FERMILAB-TM-2610-AE-CDFermi National Accelerator Laboratory, doi:10.2172/1250877
Newman, J. A., Cooper, M. C., Davis, M., et al. 2013, ApJS, 208, 5
Newton, O., Cautun, M., Jenkins, A., Frenk, C. S., & Helly, J. C. 2018, MNRAS, 479, 2853
Oemler, A., Clardy, K., Kelson, D., Walth, G., & Villanueva, E. 2017, COSMOS: Carnegie Observatories System for MultiObject Spectroscopy, Astrophysics Source Code Library, ascl:1705.001
Pace, A. B., Erkal, D., & Li, T. S. 2022, ApJ, 940, 136
Pace, A. B., Kaplinghat, M., Kirby, E., et al. 2020, MNRAS, 495, 3022
Pace, A. B., & Li, T. S. 2019, ApJ, 875, 77
Pace, A. B., & Strigari, L. E. 2019, MNRAS, 482, 3480
Patel, E., Kallivayalil, N., Garavito-Camargo, N., et al. 2020, ApJ, 893, 121
Pawlowski, M. S., McGaugh, S. S., & Jerjen, H. 2015, MNRAS, 453, 1047
Pawlowski, M. S., Pflamm-Altenburg, J., & Kroupa, P. 2012, MNRAS, 423, 1109
Pietrzyński, G., Graczyk, D., Gallenne, A., et al. 2019, Natur, 567, 200
Plummer, H. C. 1911, MNRAS, 71, 460
Price-Whelan, A. M. 2017, JOSS, 2, 388
Robin, A. C., Reylé, C., Derrière, S., & Picaud, S. 2003, A&A, 409, 523
Schlafly, E. F., & Finkbeiner, D. P. 2011, ApJ, 737, 103
Schlegel, D. J., Finkbeiner, D. P., & Davis, M. 1998, ApJ, 500, 525
Schörck, T., Christlieb, N., Cohen, J. G., et al. 2009, A&A, 507, 817
Sesar, B., Hernitschek, N., Mitrović, S., et al. 2017, AJ, 153, 204
Simon, J. D. 2018, ApJ, 863, 89
Simon, J. D. 2019, ARA&A, 57, 375
Simon, J. D., Drlica-Wagner, A., Li, T. S., et al. 2015, ApJ, 808, 95
Simon, J. D., & Geha, M. 2007, ApJ, 670, 313
Simon, J. D., Li, T. S., Drlica-Wagner, A., et al. 2017, ApJ, 838, 11
Simon, J. D., Li, T. S., Erkal, D., et al. 2020, ApJ, 892, 137
Sohn, S. T., Majewski, S. R., Muñoz, R. R., et al. 2007, ApJ, 663, 960
Starkenburg, E., Hill, V., Tolstoy, E., et al. 2010, A&A, 513, A34
Strigari, L. E. 2018, RPPh, 81, 056901
Stringer, K. M., Drlica-Wagner, A., Macri, L., et al. 2021, ApJ, 911, 109
Tonry, J. L., Denneau, L., Flewelling, H., et al. 2018, ApJ, 867, 105
Torrealba, G., Belokurov, V., & Koposov, S. E. 2019a, MNRAS, 484, 2181
Torrealba, G., Belokurov, V., Koposov, S. E., et al. 2019b, MNRAS, 488, 2743
Torrealba, G., Koposov, S. E., Belokurov, V., et al. 2016, MNRAS, 463, 712
Torrealba, G., Belokurov, V., Koposov, S. E., et al. 2018, MNRAS, 475, 5085
Trujillo, I., D'Onofrio, M., Zaritsky, D., et al. 2021, A&A, 654, A40
van der Marel, R. P., Alves, D. R., Hardy, E., & Suntzeff, N. B. 2002, AJ, 124, 2639
Vasiliev, E., Belokurov, V., & Erkal, D. 2021, MNRAS, 501, 2279
Vivas, A. K., Martínez-Vázquez, C., & Walker, A. R. 2020, ApJS, 247, 35
Walker, M. G., Mateo, M., Olszewski, E. W., et al. 2006, AJ, 131, 2114
Walsh, S. M., Jerjen, H., & Willman, B. 2007, ApJL, 662, L83
Wang, M. Y., de Boer, T., Pieres, A., et al. 2019, ApJ, 881, 118
Wang, S., & Chen, X. 2019, ApJ, 877, 116
Weisz, D. R., Koposov, S. E., Dolphin, A. E., et al. 2016, ApJ, 822, 32
Wenger, M., Ochsenbein, F., Egret, D., et al. 2000, A&AS, 143, 9
Willman, B., Blanton, M. R., West, A. A., et al. 2005, AJ, 129, 2692
Willman, B., Geha, M., Strader, J., et al. 2011, AJ, 142, 128
Willman, B., & Strader, J. 2012, AJ, 144, 76
Wolf, J., Martinez, G. D., Bullock, J. S., et al. 2010, MNRAS, 406, 1220
York, D. G., Adelman, J., Anderson, J. E., Jr., et al. 2000, AJ, 120, 1579
Youakim, K., Starkenburg, E., Martin, N. F., et al. 2020, MNRAS, 492, 4986
Zoutendijk, S. L., Brinchmann, J., Bouché, N. F., et al. 2021a, A&A, 651, A80
Zoutendijk, S. L., Júlio, M. P., Brinchmann, J., et al. 2021b, arXiv:2112.09374
Zucker, D. B., Belokurov, V., Evans, N. W., et al. 2006, ApJL, 650, L41